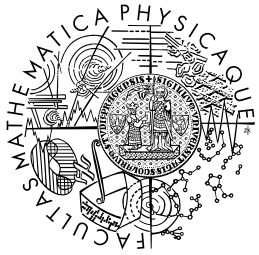

FACULTY
OF MATHEMATICS
AND PHYSICS
Charles University

MASTER THESIS

Barbora Křivská

Analysis of twin-roll cast aluminum-steel clad strips

Department of Physics of Materials

Supervisor of the master thesis:	RNDr. Michaela Šlapáková, Ph.D.
Study programme:	Physics
Study branch:	Physics of Condensed Matter and Materials

Prague 2020

I declare that I carried out this master thesis independently, and only with the cited sources, literature and other professional sources.

I understand that my work relates to the rights and obligations under the Act No. 121/2000 Sb., the Copyright Act, as amended, in particular the fact that the Charles University has the right to conclude a license agreement on the use of this work as a school work pursuant to Section 60 subsection 1 of the Copyright Act.

In Prague date ..... signature of the author

First and foremost, I would like to express my appreciation above all to my supervisor RNDr. Michaela Šlapáková, Ph.D. for introducing me to the field of electron microscopy and her guidance throughout my studies since my bachelor thesis. I would also to thank to doc. RNDr. Miroslav Cieslar, CSc. for wide-ranging consultation on how to organize and present the obtained results and for the great patience with me. My thanks also belong to bc. Lucia Bajtošová for help with the TEM in-situ analysis and prof. Mgr. Jakub Čížek, Ph.D. who provides me several positron experiments to supplement the presented study. Another thanks go to Ing. Jana Kálalová and Marta Čepová for acquainting me with the laboratory and light optical microscopy. Special thanks go to bc. Martin Kihoulou who introduced me to FEM simulations and for his never-ending support. Last but not least, I would like to thank to my family for their love and their faith in me.

Title: Analysis of twin-roll cast aluminum-steel clad strips

Author: Barbora Křivská

Department: Department of Physics of Materials

Supervisor: RNDr. Michaela Šlapáková, Ph.D., Department of Physics of Materials

Abstract: The microstructure, diffusion and phase transformations in aluminum-steel clad sheet were studied within the thesis by means of light optical microscopy, electron microscopy, resistometry and positron annihilation spectroscopy. Results of experimental methods were supplemented by finite element method employed for evaluation of electrical resistivity and simulation of diffusion between steel and aluminum. Several annealing experiments were carried out. The effective interdiffusion coefficient was evaluated by Boltzmann-Matano method from measured concentration profiles through the interface. Formation of an interfacial intermetallic phase was studied and orthorhombic phases $Al_{13}Fe_4$ and Al_5Fe_2 were identified present in the layer. Surprising results were obtained from the in-situ annealing in TEM (SEM) which go against the results found in a recent literature – the interfacial layer grows towards steel layer.

Keywords: Al–Fe clad, Twin-roll casting, diffusion, phase transformation

Contents

Introduction

Aluminum and iron alloys belong to a group of the most important engineering materials due to their exploitable properties in various applications and low material cost. Al alloys stand out among the materials in the field of engineering where low weight component or good corrosion resistance are required. Iron is the main constituent of steels, which are all-purpose materials for structural applications where high strength, good creep resistance and formability are needed.

Joining of two dissimilar materials for the purpose of formation of a composite material can bring unprecedent product characteristics beyond the ones of each conventional monomaterials [1]. The joints of steel and Al alloys seem very attractive due to the possible combination of low density of Al and high strength of steel and so the final material may be applied as a structural element in car bodies and chassis, aircraft constructions and shipbuilding. Such conjunction can also provide high thermal conductivity and thermal capacity usable in heat exchangers [2] and smelting production of Al as well as in household applications [3].

The thesis is focused on a development of a flat composite Al-steel clad material. Cladding is a procedure based on (both double- or multi-) layering of different materials with continuous bonding layers. The most common production method of the clad strips is cold or hot roll bonding, which makes more than 90 % of all flat clad products.

Nevertheless, these methods suffer from severe drawbacks – high energy and time consumption resulting in a high cost of the final product. The reason lies in the complicated preparation of substrates. Firstly, single layers of the materials are prepared (manufacturing by conventional direct chill casting and subsequent reduction by multi-pass hot rolling increase the metal sheet cost significantly). Then the substrate must be properly cleaned, ground and (in some cases) coated. Al these procedures also increase the final price of the material.

Possible solution how to overcome these drawbacks is twin-roll casting where the intermediate heating is not needed. Twin-roll casting can be used for both manufacturing of multilayered clad strips directly from melts of different metals and using melt of the one metal together with a solidified sheet of the other one. TRC is supposed to be energy and material saving method and moreover, the presence of detrimental impurities appearing on the interfaces should be reduced [2].

Overview of studied topics

1.1 Clad materials

Cladding is essentially a joining of two or more layers of different metals. Metallic clad composites have been widely used in industries as well as for household applications. They can be produced in miscellaneous forms - as strip, foil, tube, rod or wire [4]. Cladding can provide many solutions in either functionality or cost saving as well as both of them. Different clad materials could be applied in structural applications as materials enhancing strength-to-weight ratio, in thermomechanical control, electrical or in corrosion resistant applications where a relatively inexpensive base metal could be covered with a corrosion resistant metal on the surface [5]. Particular example worthy of notice is nuclear cladding where current research and development efforts have focused on reducing the oxidation corrosion caused by a high-temperature steam and employing corrosion-resistant coatings of zirconium alloys by more oxidation-resistance materials such as FeCrAl alloys [6].

Another example of application is cladding of rails. Material degradation in the form of wear or rolling contact fatigue in the railhead often developed as a result of the contact between train wheels and rail tracks [7]. A possible solution presented by Lai et al. [8, 9] is laser cladding technique for both production of new premium rails of extended longevity and reparation of a damaged section of the rail track. A representative of the structural material is Ti-clad steel providing good mechanical properties of structural carbon steel and excellent corrosion and impact resistance of titanium in a symbiotic fashion [10]. Excellent corrosion resistance enables to spread utilization of this type of composite material to petrochemical industries and ocean engineering [11].

One more functional combination of different metals is Ni/304StainlessSteel/Cu clad composite used for a bottom battery cap, where the outer Ni surface layer provides low contact resistance, atmospheric corrosion resistance and cosmetic appearance; thick stainless steel in the core is for strength and deep drawing, perforation corrosion resistance and total low cost; and inner Cu surface layer provides an electrode contact surface for electrochemical cell performance [5].

This thesis deals with Al-clad steel strips, which also represent a significant part of structural materials. Great advantage of this joint is a combination of the low cost and dissimilar attractive properties of both metals. Aluminum belongs to the group of materials extensively used for corrosion protection. The single largest application for cold roll-bonded Al/StainlessSteel clad composite is a production of automotive trims, which provides corrosion protection to the

car body while preserving a bright corrosion-resistant surface [4]. Apart from the corrosion resistance, the aluminum heat exchange performance could be used for a production of refrigerators parts or energy-saving cookware. High strength of a steel with a low weight of an aluminum also finds employment in a production of track bumpers.

1.2 Cladding Methods

1.2.1 Fusion welding

Fusion welding is a joining process using melting of the base metal to make the weld. This method is mostly used to join materials of a similar composition and melting temperatures [12]. There are several ways to create a weld pool of molten metal – arc welding, electron beam and laser welding are commonly used to connect a wide range of metals. A joining of dissimilar materials is often accompanied by a formation of high concentrations of intermetallic phases which could be detrimental for the joint. In case of Al-steel joint, a thick layer of brittle Al-rich intermetallics (e.g. Al_5Fe_2, $Al_{13}Fe_4$) forms on the interface and so a possible rupture of the joint can occur under stress [13].

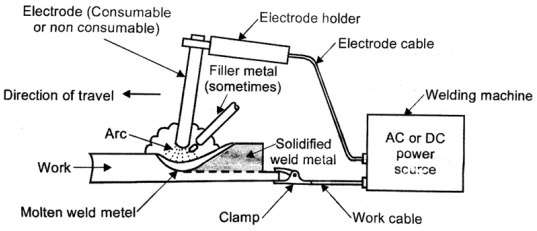

(a) Arc welding [14]

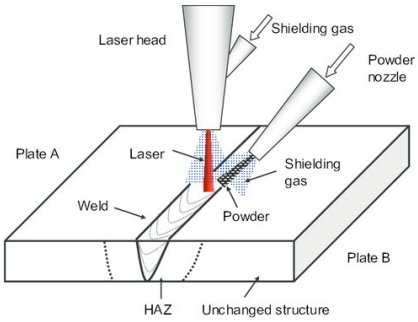

(b) Laser beam welding [15]

Figure 1.1: Schemes of two fusion welding methods. Arc welding consists of an electric arc established to melt the surface of substrate material, usually in a shielded gas environment. Laser cladding uses the same concept, except that a laser is used to melt the surface of the substrate instead of arc. Addition material can be supplement in the form of a wire, powder or a strip in both arc and laser beam welding.

1.2.2 Explosive cladding

Explosion welding is one of the solid-state techniques of the metal cladding [16]. It can be considered as a kind of hot-pressing, in which controlled explosive detonations force two or more metals together at high pressures [17]. The joining parts are arranged toward each other at an angle of 1–15°, depending on the material and method, and are prepared with a layer of explosive on the top. After ignition the joining areas are moved against each other at a high speed. Joining happens continuously by a local plastic deformation of the contact area

(scheme of the explosive cladding is displayed in Figure 1.2a). The joint is caused by a deformation-induced melting bath. The dilution of the molten zones then results in plane or corrugated interfaces [18]. A form of a possible wavy bond is displayed in Figure 1.2b). An advantage of explosive welding is the possibility of

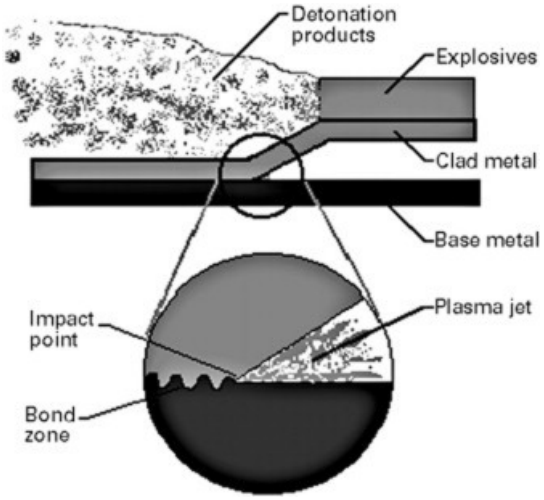

(a) Scheme of explosive welding process [19]

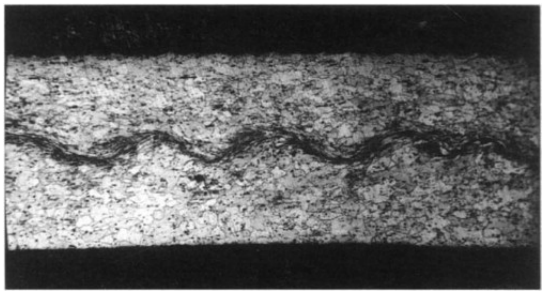

(b) Wavy bond structure obtained by explosive welding [17]

Figure 1.2: Explosive cladding.

making sheets and plates of large sizes with a high productivity rate. Moreover, the very short time of the process excludes the formation of thick interface layers of brittle intermetallic phases [17]. Unfortunately, no matter how interesting process from a technological view the explosive welding is, it certainly does not rank among the environmentally friendly cladding methods.

1.2.3 Friction stir welding and brazing

Friction stir welding (FSW) belongs to new solid-state joining processes invented in 1991 at The Welding Institute of UK [20]. In particular, it can be used to join high-strength aerospace aluminum alloys and other metallic alloys that are hard to weld by a conventional fusion welding [21]. The technique is based on a rotation of a non-consumable tool with a specially designed pin. Heating is achieved by a friction between the tool and the workpiece and by plastic deformation of the workpiece. During FSW process, the material undergoes intense plastic deformation at elevated temperature leading to a formation of a fine and equiaxed grain structure in the weld region [22, 23], which contributes to obtaining of good mechanical properties of the final product. Additionally, FSW is deemed to be amongst the most "green" technology due to its energy efficiency, environment friendliness and versatility [21].

Using friction stir welding for dissimilar joining between aluminum and steel is of interest because the formation of brittle intermetallics could be suppressed since no melting of both base metals take place. Addition of Zn coating of the steel can be used to enhance the intimate contact or effectual mutual diffusion

between the parent metal [24, 25]. However, the case of Al cladding of the non-galvanized steel (without the presence of Zn coating) could suffer from following problems: a damage of the pin tip, voids along the interface that grows with an increasing pin depth, formation of the intermetallic compounds as a consequence of a direct mixing of Al and steel [24, 26, 27]. A solution was proposed by Zhang et al. who modified a tool by replacing the pin for joining Al to metals of high hardness. The procedure is now known as friction stir brazing [28, 29]. A scheme of both friction stir welding and brazing are displayed in the Figure 1.3.

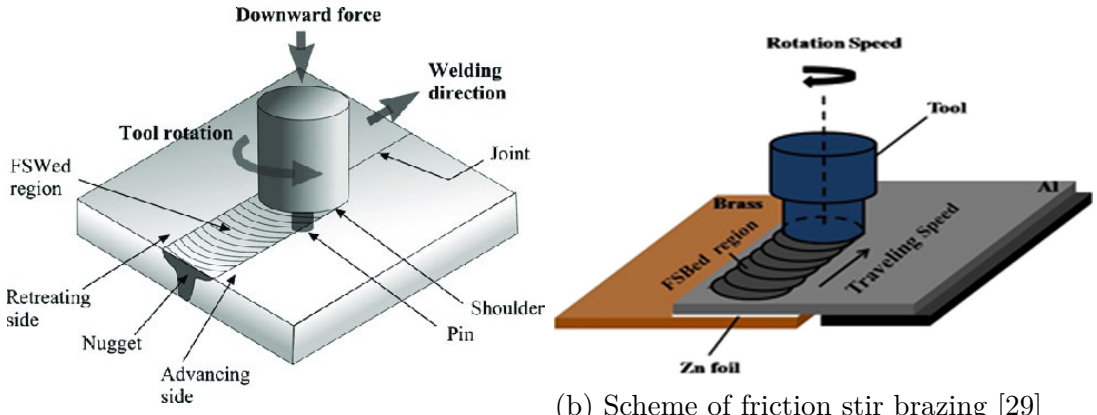

(a) Scheme of friction stir welding [30]

(b) Scheme of friction stir brazing [29]

Figure 1.3: Friction stir welding and brazing

1.2.4 Roll bonding

Roll-bonding also belongs to the group of solid-state welding methods providing the possibility of combination either similar or dissimilar metals without melting. The metallic sheets are joined using a high pressure between the rolls at intermediate temperatures. Scheme of the roll-bonding process is displayed in Figure 1.4.

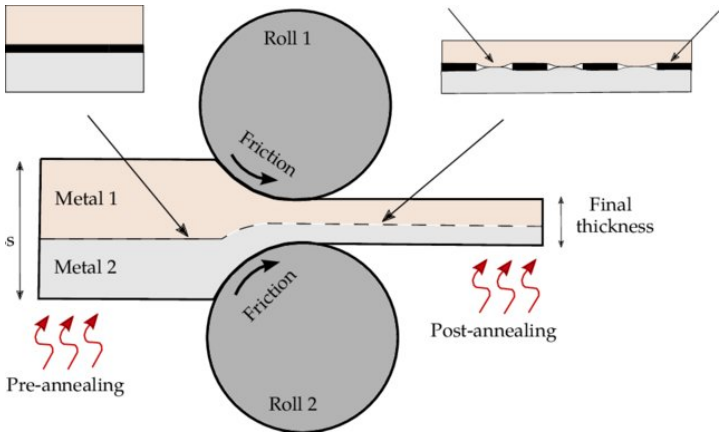

Figure 1.4: Scheme of roll-bonding process [31]

1.2.5 Twin-roll casting

The thesis concerns a production of Al-steel clad sheets by twin-roll casting since this method offers an opportunity how to produce bimetallic strips on a large scale with a low energy consumption.

The first reference about a direct casting of bi-metal structures is available from the US patent from E. B. Hudson, who published the principles of the special continuous caster in 1938. One metal is fed on the roll's surfaces and so create the outer shell of the strip. The other metal is fed internally and comes into contact with the thin outer shell and form the core of the final bi-metal strip [32].

In 1997, Papich et al. published the method of horizontal twin-roll casting of the cladded material using combination of previously solidified sheet of the first metal and the melt of the second material [33]. The production was tested on different Al alloys. A higher strength was shown compared to hot roll-bonded composites. An experiment with a joining of two different metals (Al and Mg alloys) were performed by Rao and Bae et al. [34, 35] and intermetallic phases on the interface of the materials were investigated.

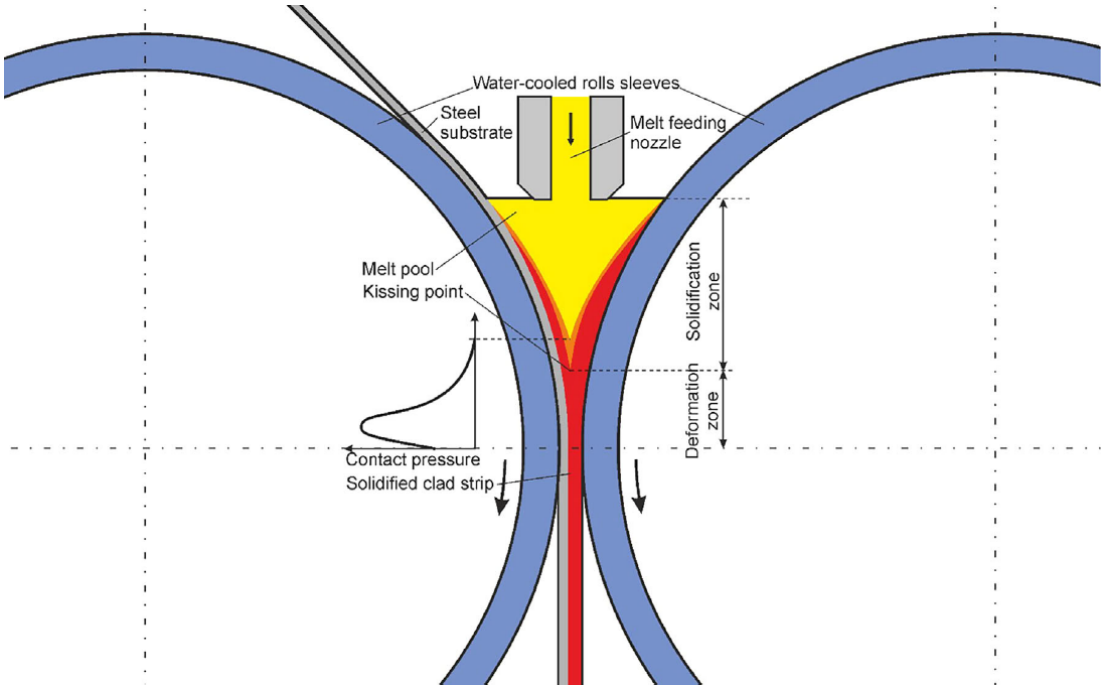

Figure 1.5: Scheme of twin-roll casting of clad strips [36]

1.3 Phase composition of the interface region

Phase composition and thickness of an intermetallic layer depends on casting parameters as well as on subsequent heat treatment, because the process of interdiffusion is accelerated at higher temperatures.

Akramifard et al. studied the microstructure and mechanical properties of the three-layer AA1050/304L/AA1050 composite produced by cold-roll bonding process [37]. Parent alloys has very similar chemical composition as the alloys which were joined by twin-roll casting and studied in this thesis: 304L grade of steel is a low carbon variant of the steel of 304 grade (C content should not exceed 0.03 wt.% [38]) and aluminum alloy AA 1050 is also a commercially pure aluminum alloy. The roll-bonding process was carried out at room temperature and at 100 °C, as the temperature strongly influences the resulting microstructure on the steel layer. It was reported, elevated temperatures 100 °C hindered a strain induced austenite-martensite transformation, so the austenite microstructure of 304L was preserved. An isothermal one-hour-lasting post-annealing treatment was conducted as it activates recovery or recrystallization of the Al layer and interdiffusion in the interface region. Growth of the intermetallic layer on the Al-steel interface was not observed up to 400 °C / 1 h annealing. About 2.6 μm thick intermetallic layer was found on the interface after annealing at 500 °C / 1 h. Annealing at 600 °C / 1 h caused an enormous growth of the interfacial layer which thickness reached from 9 to 17 μm. However, the excessive growth of the intermetallic phase was connected with cracks that propagated along Al-intermetallic phase interface and so resulted in very poor bond (easily detachable even by hand). According to X-ray diffraction results of, the interfacial layer was composed of Fe_4Al_{13}, FeC and Al_8SiC_7 phases. Other detected phases present either on the interface or in the individual layers: $FeAl_2$, Al_3Ni_2, Al_5FeNi, Cr_7C_3, Al_20_3, Al_2Mn_3, Al_8Cr_5, Al_3Fe and Fe_20_3 were detected.

Another contribution to the phase analysis belongs to Ryabov et al. [39] who studied the formation of intermetallic phases on the Al-Fe interface during annealing. Phases of the following stoichiometries were found: Fe_4Al_{13} (of the highest thermal stability), Fe_2Al_5, $FeAl_2$, FeAl, Fe_3Al were found. In addition, a maximal thickness ~ 5 μm of intermetallic layer, when the composite is of a good quality, was determined. Wagner et al. established that high percentage of Fe_4Al_{13} deteriorates mechanical properties of the clad strip because of its high brittleness [40].

Another parameter influencing the resulting thickness of the intermetallic layer is a choice of alloying elements and their amounts. Springer et al. [3] studied the influence of Si content in an Al alloy on the thickness of the intermetallics formed on the interface of an Al alloy and a low carbon steel. Three types of diffusional experiments of Al-steel joining were performed: solid-solid at 600 °C, semi/solid-solid, solid-liquid at 675 °C. All experiments were carried out in Ar atmosphere and in the case of solid-liquid joining, the steel layer was coated by Zn to enhance a wettability for the Al-melt. The results were obtained for pure aluminum and Al-5wt.%Si alloy. It was shown, that the most significant phase present in the interfacial layer was Fe_2Al_5 phase with a typical columnar grain shape structure. Another phases analyzed by SAED in TEM were also proposed. In all diffusional experiments, a parabolic growth of the Fe_2Al_5 phase

was observed and it was shown that the effect of Si content is rather opposite for the solid-solid experiments then for the solid-liquid one.

Generally, the optimal casting parameters including a choice of alloying elements and a subsequent heat treatment should be determine to obtain thin continuous diffusion seam. The aim of the presented work is to analyze the interface zone structure during both isothermal and isochronal annealing by means of scanning electron microscopy, transmission electron microscopy coupled with resistometrical measurements. A monitoring of diffusional processes in the Fe-Al system at elevated temperatures could help to extend the application of twin-roll casting to the production of bi-metal clad sheets.

Background for simulations

2.1 Diffusion

During twin-roll casting of Al-steel clad sheets, a very thin diffusional layer forms on the interface of aluminum and steel. Its thickness and phase composition is a crucial parameter that influences the bonding strength between the metals and so determine mechanical properties of the final clad strip. The following section concern an overview of elementary and equations used in the thesis.

2.1.1 Diffusion mechanism in metals

The possibility of atom motion in a crystalline solid is a bit limited due to an ordering of atoms in a periodic lattice. Nowadays, there are several theories describing the mechanism how the atom can get from its position to another one. Historically, the first concept of atom motion was a simple exchange or ring mechanism, where two (or more atoms placed in a circle) move together and exchange their positions. However, since the activation energy of one step of the exchange mechanism is very high, the probability that this type of atom motion occurs is rather negligible [41].

Another proposed mechanism is an interstitial mechanism, where atoms can move directly from one interstitial site to another. But there is a big restriction on the atom size - only small atoms can get through the lattice by that way. Indirect interstitial mechanism, described as pushing of the site lattice atom by an interstitial into an interstitial position so the interstitial fill its site allowing a substitutional diffusion, has a similar limitation on a size of the interstitial as in the previous mechanism.

Since the crystal structure is not perfectly arranged at temperatures above 0 K and there is certain amount of vacancies in the material, the vacancy mechanism is energetically the most convenient way of the atom flux. As the atom jumps into a neighboring vacancy, a new vacancy is created and another atom in the vicinity of the new vacancy can move. In comparison with diffusion mechanisms mentioned above, vacancy-assisted diffusion allows atoms of different elements to move with different rates. The phenomenon of different diffusional velocities was firstly shown and described by Kirkendall in 1947 [42].

2.1.2 Kirkendall effect

The first experiment revealing difference of diffusional fluxes of two types of atoms was conducted by Ernest Kirkendall and Alice Smigelskas in the 1940's. The studied material was a marked diffusional couple cooper-brass: Mo wires (acting as markers of an initial interface) were stretched along a polished brass (70wt.%Cu-30wt.%Zn) and then it covered by pure Cu. The specimen was annealed at 785 °C for several days. During annealing the motion of Mo wires was determined out by measurements of a distance between the opposite wires.

Motion of the marker was described as a result of the difference between Zn and Cu fluxes - Zn atoms escaped faster from the brass core than the Cu atoms were able to replace them. On a macroscopic scale, decrease of the distance between the opposite Mo markers was observed.

2.1.3 Fick's laws

The first mathematical description of diffusion processes was proposed by Adolph Fick in 1855 [43]. Fick's first law express a direct proportion between a flux J and the gradient of concentration c [44, 45]

$$\vec{J} = -D\nabla c, \tag{2.1}$$

where D is a diffusion coefficient.

Fick's second law (also known as diffusion equation) is derived from the principle of mass conservation with applying of Fick's fist law and the divergence theorem

$$\frac{\partial c(x,t)}{\partial t} = \nabla(D\nabla c) = D\Delta c(x,t), \tag{2.2}$$

where x is a coordinate.

2.1.4 Interdiffusion

Generally, the diffusion flux need not be proportional to the concentration gradient as it is stated by the first Fick's law. A determinative factor is the gradient of chemical potential, which is proportional to the concentration gradient only for dilute systems or ideal solid solution [46]. Moreover, concerning dilute binary alloy, a different diffusional rate of the atoms A and B is not unusual. The differing diffusional fluxes are macroscopically observed as the above mentioned Kirkendall effect.

Intermixing of the (dilute) binary A-B system could be described by an interdiffusion coefficient, which commonly depends on the concentration. The interdiffusion coefficient could be determined by Boltzmann-Matano method, which is based on an inverting of the second Fick's law.

Boltzmann-Matano method

Mehrer showed the derivation of Boltzmann and Matano in [46]. The derivation is included in the thesis, since it explains the princip of the determination of the diffusion coefficient.

The non-linear partial differential equation 2.2 can be transform to a nonlinear ordinary differential equation by using a new variable

$$\eta = \frac{x - x_M}{2\sqrt{t}}, \tag{2.3}$$

where x_M denotes a special reference plane, so-called Matano plane, which will be defined later.

Using of the variable η brings a new differential operator $\frac{d}{d\eta}$, which is related to the partial differential operators by following equations

$$\frac{\partial}{\partial x} = \frac{d}{d\eta}\frac{\partial \eta}{\partial x} = \frac{1}{2\sqrt{t}}\frac{d}{d\eta}, \tag{2.4}$$

$$\frac{\partial}{\partial t} = \frac{d}{d\eta}\frac{\partial \eta}{\partial t} = -\frac{\eta}{2t}\frac{d}{d\eta}. \tag{2.5}$$

By applying of these operators in equation 2.2 (in 1D) we obtain Fick's second law as an ordinary differential equation for $c(\eta)$

$$-2\eta\frac{dc}{d\eta} = \frac{d}{d\eta}\left(D(c)\frac{dc}{d\eta}\right). \tag{2.6}$$

We assume a semi-infinite diffusional couple (e.g. joined semi-infinite bars) with the initial concentration conditions

$$c(x, t = 0) = c_L, \quad x < 0 \tag{2.7}$$

$$c(x, t = 0) = c_R, \quad x > 0 \tag{2.8}$$

From a concentration profile $c(x,t)$ after a diffusion annealing lasting certain time t, the diffusion coefficient can be determined for fixed concentration c^* by following way. Integration obtained from equation 2.6 between c_L and c^* yields

$$-2\int_{c_L}^{c^*} \eta dc = \left[D(c)\frac{dc}{d\eta}\right]_{c_L}^{c^*} = D(c^*)\frac{dc}{d\eta}\bigg|_{c^*} - D(c_L)\frac{dc}{d\eta}\bigg|_{c_L}. \tag{2.9}$$

Assumption of semi-infinite diffusional couple leads to a vanishing of concentration gradient when c reaches c_L or c_R, so we obtain the diffusional coefficient for the fixed c^*

$$D(c^*) = \frac{-2\int_{c_L}^{c^*} \eta dc}{\frac{dc}{d\eta}|_{c^*}}. \tag{2.10}$$

Transform back to the original space and time coordinates yields

$$D(c^*) = \frac{-2\int_{c_L}^{c^*} \frac{x - x_M}{2\sqrt{t}} dc}{\frac{dc}{dx}|_{c^*} 2\sqrt{t}} = -\frac{1}{2t}\frac{\int_{c_L}^{c^*}(x - x_M)dc}{\frac{dc}{dx}|_{c^*}}. \tag{2.11}$$

Position of the reference Matano plane results from a conservation condition which says that the gain of the diffusing species found on the left-hand side must have enter by diffusion from the right-hand side

$$\int_{-\infty}^{x_M} [c(x) - c_L]dx = \int_{x_M}^{\infty} [c_R - c(x)]dx. \tag{2.12}$$

Changing of the integration over space to integration over concentration we obtain

$$(c_L - c_R)x_M + \int_{c_L}^{c_M} x(c)dc + \int_{c_M}^{c_R} x(c)dc = 0, \tag{2.13}$$

where the first term vanishes if the Matano plane is chosen as the origin of the x-axes. Position of the Matano plane is determined from the measured concentration profile by comparing the filled areas in the Figure 2.1.

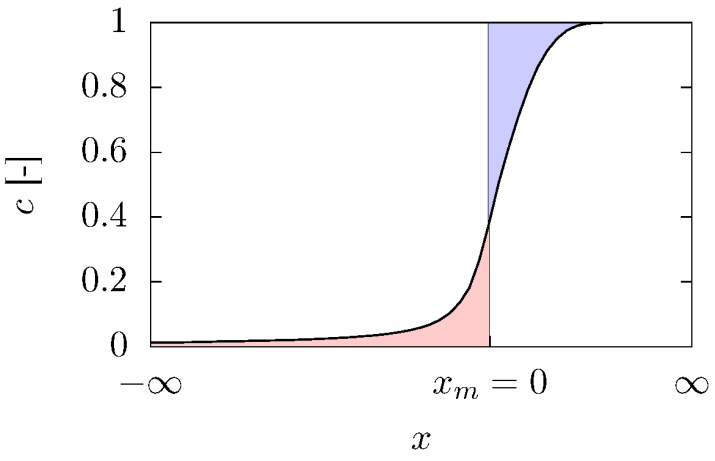

Figure 2.1: Matano plane in the error-function-concentration profile.

2.1.5 Simulation of diffusion using finite element method

Concentration profiles $c(x)$ obtained by EDS line analysis in SEM should be smooth (e.g. with Savitzky-Golay filter [47]) for calculation of the diffusion coefficient according to equation 2.11, since a $c(x)$ derivative acts as the denominator. The program for diffusion simulation was developed using freely available FEniCS software, which is designed for numerical solving of partial differential equations by finite element method [48, 49].

Because of low values of $D(c)$ (order of 10^{-18}), 1D diffusion equation was modified to a nondimensionalized form. For concentration function linear Lagrange elements are used. For time discretization Crank-Nicolson semi-implicit scheme [50] with Courant–Friedrichs–Lewy condition [51] were used. Diffusion coefficient can be for simple cases approximated by constant D, however for more complicated profiles we approximate it by piecewise constant function $D(c)$. Since the term $D(c)$ brings nonlinearity to the equation, it was linearized by means of the previous time step. Resolution of 400 nodes was find sufficient for all calculations.

2.2 Determination of the material resistivity

Manesh [52] pursued the bonding strength between the layers of aluminum steel clad sheet via peeling test and four point probe test. The clad composite in his study was prepared using a cold roll-bonding method. Several Al/steel/Al "sandwiches" of different thickness reductions were obtained, which were subsequently subjected to peeling and resistometrical testing. It was found that theoretical value of the composite effective resistivity ρ_{clad} calculated from resistivities of Al and steel layers ρ_{Al}, ρ_{steel} and their volume fractions v_{Al}, v_{steel}

$$\frac{1}{\rho_{\text{clad}}} = \frac{v_{\text{Al}}}{\rho_{\text{Al}}} + \frac{v_{\text{steel}}}{\rho_{\text{steel}}} + \frac{v_{\text{Al}}}{\rho_{\text{Al}}}. \tag{2.14}$$

never equals to the measured one. It was explained by non-consideration of the "bond-resistance" in the calculation of the theoretical resistivity value. Therefore, the difference between the measured ρ_m and predicted ρ_p effective resistivity values $\Delta\rho = \rho_m - \rho_p$ may be considered as an inherent resistivity of the bond width. By calibration of the resistometrical data via the corresponding peeling test results, the resistivity measurement could serve as a non-destructive method for the bond strength evaluation.

A theoretical value of the effective clad sample resistivity could be calculated from the resistivities of the individual materials, which should also be investigated concurrently with the clad sheet during all annealing experiments. The influence of electrical field inhomogeneity inside the sample volume was solved by finite element method (FEM). The main error source is the uncertainty of determination of the sample geometry and physical realisation of the sample contacts.

2.2.1 Theoretical background

Ohm's law in a differential form states that electrical current density $\vec{j}$ in a conductor is directly proportional to the electric field $\vec{E}$

$$\vec{E} = \rho\vec{j}, \tag{2.15}$$

where the constant of proportionality ρ is the electrical resistivity of the material.

The current density $\vec{j}$ satisfies a continuity equation. In the electroquasistatic approximation, it holds

$$\nabla \cdot \vec{j} = 0. \tag{2.16}$$

Since a direct current (DC) electrical circuit is of interest, electric field $\vec{E}$ is irrotational, so it can be expressed by electrical potential ϕ

$$\vec{E} = -\nabla\phi. \tag{2.17}$$

Substituting $\vec{j}$ in the continuity equation 2.16 from the Ohm's law 2.15 and the identity 2.17 one can obtain

$$\nabla \cdot \frac{1}{\rho}\nabla\phi = 0. \tag{2.18}$$

A uniform conductor with a homogeneous resistivity ρ then satisfies Laplace equation

$$\Delta\phi = 0, \tag{2.19}$$

with suitable Dirichler or Neumann boundary conditions

$$\phi(x) = \phi_D, x \in \Gamma_1 \tag{2.20}$$

or

$$\frac{\partial \phi}{\partial \vec{n}}(x) = \rho \vec{j}, x \in \Gamma_2 \tag{2.21}$$

with

$$\frac{\partial \phi}{\partial \vec{n}}(x) = 0, \text{elsewhere.} \tag{2.22}$$

2.2.2 Simulation of electric potential using finite element method

The program for calculation of the electrical potential ϕ in the sample was also developed using FEniCS software. Three-dimensional mesh representing the H-sample with at least 100,000 tetrahedral elements was constructed to ensure adequate accuracy of the numerical model. In the following section, weak formulation of the problem is derived.

2.2.3 Governing equations

Multiplying the bulk Laplace equation 2.19 by a test function $\delta\phi$, integrating over the spatial domain Ω representing the H-sample, and integrating by parts yields the weak formulation

$$\int_\Omega (\nabla \cdot \nabla \phi) \delta\phi \, dx = \int_{\delta\Omega} \vec{n} \cdot \nabla\phi \delta\phi \, dS - \int_\Omega \nabla\phi \cdot \nabla\delta\phi \, dx = 0. \tag{2.23}$$

First of all, the problem was solved using Dirichlet boundary conditions

$$\phi(x) = 0, x \in \Gamma_1, \phi(x) = 1, x \in \Gamma_2, \tag{2.24}$$

where Γ_1 and Γ_2 denotes boundaries where the H-sample is connected to the current source by alligatigator clamps (see Figure 2.2). This shows the influence of the sample shape on a spatial distribution of the electrical potential and reveals the inhomogeneities of the electrical field near the sample "legs" and the alligators clamps.

During resistometrical measurements, voltage was measured between the clamps attached to the opposite sample legs (marked with A_1 and A_2 in Figure 2.2). The value of the potential drop between the same points X and Y was also read from the solution of the FEM simulation. These measured and calculated values were then compared so the simulation could be re-scaled for a real sample.

Real values of the electrical potential served for calculation of the material resistivity. Since the electrical current was set on 0.1 A, electrical potential distribution $\phi(x)$ was calculated and a macroscopically homogeneous sample was assumed, the electrical resistivity could be obtained from equations 2.15 and 2.17 enumerated in the middle of the H-sample where the electric field is the most homogeneous and so the current density could be easily determined as a division of the electrical current and the sample cross-section

$$j = \frac{I}{wd}, \tag{2.25}$$

where w and d are the dimensions of the cross-section.

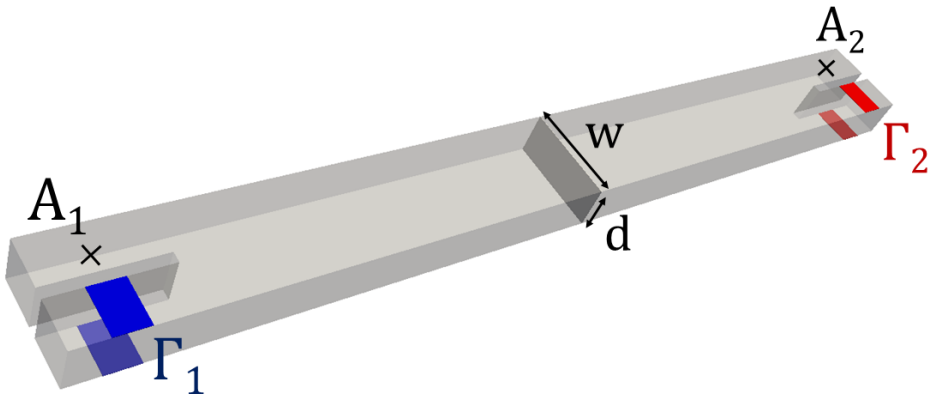

Figure 2.2: Computational domain representing the H-shape sample with highlighted boundaries.

Material and experimental methods

3.1 Material

Aluminum-steel clad sheets were produced by means of twin-roll casting at the University of Paderborn. The laboratory twin-roll caster is equipped with two water-cooled rolls with a diameter of 370 mm and a length of 200 mm. A casting process was realized with a vertical operation plane. A solid austenitic steel (type 1.4301) strip with a thickness of 0.5 mm was fed into a gap between the rolls simultaneously with the melt of a technical pure aluminum EN AW-1070 (scheme of the process can be seen in the previous chapter in the Figure 1.5). A chemical composition of each layer is displayed in the Table 3.1.

Table 3.1: Chemical composition of clad composite layers in given by norm wt.%

EN AW-1070, [53]	Al	Fe	Si	Zn	Mn	Ti
Composition	>99.7	<0.25	<0.2	<0.07	<0.03	<0.03
steel 1.4301, [54]	Fe	C	Cr	Ni	Mn	Si
Composition	Balance	0.07	17.5–19.5	8.0–10.5	2	0.75

No mold release coating was applied on the roll surface either before or during the casting process. Additional casting parameters are provided in the Table 3.2. More details about the experimental twin-roll caster and its equipment can be found in [55].

Table 3.2: TRC parameters used for manufacturing of the Al-steel clad sheet

Parameter		
Melt temperature	675	°C
Casting rate	4.4	m/min
Strip thickness	2.5	mm
Cooling water's flow rate	115	l/min

Solidification of the aluminum melt is influenced by a presence of the steel strip on one side which behaves as an additional thermal barrier between the melt and

the cooled roll so a shift of the metallurgical center of solidified aluminum occurs [56]. A layer of the solidified aluminum grows from the side of the uncovered roll and the steel substrate up to so-called "kissing point" that indicates the beginning of the deformation zone, where the metal sheet yields to a thickness reduction. Final thickness of the clad strip is 2.5 mm.

In comparison to conventional roll-bonding, a flat grain structure of the aluminum substrate could be partially suppressed by the process of twin-roll cladding. This feature could influence the resulting mechanical properties. Moreover, a corrosion resistance could be strongly dependent on the grain boundary arrangement, especially if a different and more prone type of Al alloy would be used for cladding of the steel strip.

Because several authors [36, 57, 3] mention that the formation of an interfacial layer of Al-Fe intermetallic phases could influence the bonding strength and other material properties of the composite, an effect of additional high-temperature treatment of the twin-roll clad strip was studied. An experimental isochronal and isothermal annealing in a laboratory air furnace was performed and the microstructural evolution was monitored by means of experimental methods introduced in the following paragraph.

3.2 Experimental methods

3.2.1 Heat treatment

Twin-roll casting of the Al-steel clad sheet could be followed by subsequent heat treatment, which can provide additional improvement or modification of the material properties. High temperature procedures generally accelerate the diffusional processes, therefore experimental annealing was performed to explore both the diffusional processes on the interfacial part of the composite and transformations of the primary phases in the Al layer.

Isochronal and isothermal heating scheme were used. Isochronal annealing was realized with step 50 °C/ 25 min up to 600 °C. Isothermal annealing was performed at temperatures 450 °Cand 500 °C. During isothermal annealing the state of the material was monitored logarithmically - after annealing 0.25 h, 0.5 h, 1 h, 2 h, etc. up to a total annealing time 32 h. The heating schemes are graphically represent in Figure 3.1.

Before the particular annealing step for both isochronal and isothermal heating scheme, the air furnace was preheated to a required temperature. Then, samples were inserted into the furnace and annealed. Between each two annealing steps the samples were water-quenched.

3.2.2 Resistometry

Electrical resistivity measurement is widely used experimental technique for a determination of the defect amount in the material. A process of solutes redistribution, phase transformation or even short and long-range ordering can be monitored during annealing by this method. A direct current four-point probe [58] of a typical H-shape sample has been used as the lead wire resistance was

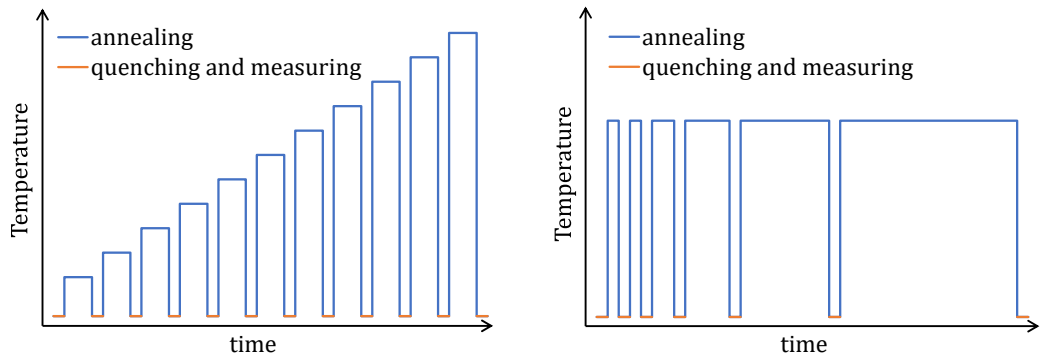

(a) Isochronal annealing (b) Isothermal annealing

Figure 3.1: Heating schemes

not negligible in comparison to the sample resistance. A scheme of the four-point circuit is displayed in Figure 3.2.

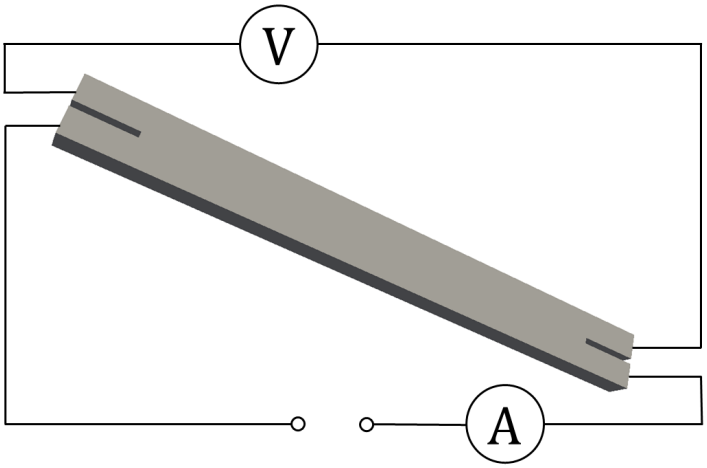

Figure 3.2: Scheme of four-point method wiring for H shape sample.

The basic principle of resistance R measurement is based on Ohm's law

$$R = U/I, \tag{3.1}$$

where I is electric current flowing through the conductor and U is a potential difference (voltage) on the conductor.

The applied current I was 0.1 A. In order to eliminate contact potentials between the sample and alligator clips used for wiring of the sample, N measurements of the voltage (denoted by U_i) were done with currents flowing in opposite directions so the resulting voltage U was determined as

$$U = \frac{1}{N} \sum_{n=1}^{N} |U_i|. \tag{3.2}$$

The inner property of the material is electrical resistivity ρ which is connected with the resistance of the sample R over a geometrical factor

$$R = f\rho. \tag{3.3}$$

Matthiesen rule [59] for a dilute alloy says, that the resistivity $\rho(T)$ can be decomposed on two parts

$$\rho(T) = \rho_{ph}(T) + \rho_i, \tag{3.4}$$

where $\rho_{ph}(T)$ is a temperature-dependent contribution of phonon excitations and ρ_i temperature independent part related to electron scattering on impurities and lattice defects.

For revealing the temperature independent part of the resistivity, the measurements were performed in a liquid nitrogen at 77 K. Relative changes of the resistivity normalized by its initial value $\frac{\Delta\rho(T)}{\rho_0}$ were calculated. In fact, an accurate estimation of the material resistivity $\rho(T)$ is difficult because of the determination of the geometrical factor. Nevertheless, estimation of the quantity $\frac{\Delta\rho(T)}{\rho_0}$ can be simplified, when the form factor of the sample is assumed to be preserved during annealing

$$\frac{\Delta R(T)}{R_0} = \frac{f\rho(T) - f\rho_0}{f\rho_0} = \frac{\rho(T) - \rho_0}{\rho_0} = \frac{\Delta\rho(T)}{\rho_0}. \tag{3.5}$$

Moreover, the residual resistivity ratio (RRR) was determined. RRR is defined as a ratio of electrical resistance at room temperature to that at 0 K, which is usually replaced by a liquid helium temperature (4.2 K). Yin et al. showed that resistance of an Al sample was nearly constant up to 20 K and changed only slightly under 77 K [60]. Due to this only subtle deviation, the RRR calculation was done from the resistivities at RT (measured in ethanol at 20 °C) and at the temperature of liquid nitrogen at 77 K (-196 °C)

$$RRR = \frac{R_{20^\circ\mathrm{C}}}{R_{-196^\circ\mathrm{C}}}, \tag{3.6}$$

where $R_{20^\circ\mathrm{C}}$ is the sample resistance measured in ethanol at room temperature and $R_{-196^\circ\mathrm{C}}$ is the resistance of the sample immersed in liquid nitrogen.

Since the RRR is measured on the same sample it nearby does not depend on its shape and sizes. Therefore direct comparison of different samples could be done. Furthermore, for dilute aluminum alloys, the evolution of RRR is similar to that observed for electrical conductivity and there is a correspondence between the absolute value of RRR and the amount of solute atoms - a higher RRR value is a sign of a higher purity of the matrix (solute atoms comprise precipitates or primary phases)[61].

In the case of investigations of solutes redistributions in alloys, phase transformations or short- and long-range ordering, it is often sufficient to deal with relative changes of the electrical resistivity. In the case of studied Al-steel clad composite, it could be seminal to determine the absolute resistivity values of the individual aluminum and steel layer, so a theoretical value of the composite sample resistance could be evaluated and compared with the measured one. Evolution of a possible difference between calculated and measured values during

annealing could be in some way connected with phase transformations on the Al-steel interface and therefore with the resulting bond strength between the layers [52]. Therefore, the resistometrical measurements of the individual aluminum and steel materials were carried out concurrently with the measurement of the clad sample during all annealing experiments. Resistivities of both monomaterials were find out by FEM and served for the estimation of the theoretical value of the composite's resistivity.

3.2.3 Light optical microscopy

Light optical microscopy (LOM) observations were performed using Zeiss Axio Observer metallographic microscope to obtain global information about the material microstructure. Especially the primary particles distribution and transformations and evolution of intermetallic Al-Fe phases on the interface during annealing experiment were studied.

Samples were cut by Struers circular saw. Approximately 0.5 cm wide strips were cut in the rolling direction (RD) from the clad sheet. Samples of a length of about 1 cm were then prepared from these strips.

Thereafter, samples were subjected to the annealing experiment in a specified heating scheme simultaneously with the samples used for resistometrical measurements. One sample was taken in each step of experimental annealing, so the microstructural changes during heating could be monitored.

Subsequently, samples were embedded in an acrylic cold mounting resin ClaroCit which enabled to keep a plane during grinding as the soft aluminum side of the sample yields faster to the grinding than the hard steel side. Grinding of the samples surface perpendicular to transversal direction (TD) was performed using SiC papers up to grit number 2000 (grain size 10 μm) and then was followed by polishing on diamond suspensions with the last suspension containing diamond particles with the size of 1 μm. Final polishing with a slight etching effect was carried out using standard colloidal silica suspension with a particle size of 0.25 μm.

3.2.4 Scanning electron microscopy

Scanning electron microscopy (SEM) could reveal the phase distribution, particle size as well as the grain size. By detecting the back-scattered electrons (BSE) a chemical contrast is revealed since more electrons are scattered by atoms of elements with a higher atomic number. Moreover, if the sample surface is polished sufficiently, individual (sub)grains could be distinguish by a channeling contrast.

Used scanning electron microscope Quanta 200F is equipped with energy-dispersive X-ray detector (EDS) and electron back-scatter detector (EBSD), so the chemical composition of the interfacial layer and crystallographic orientation analysis of the aluminum and steel layer as well as the intermediate layer could be investigated. The accelerating voltage was set at 10 kV.

The same samples as for LOM observations were used for analysis by SEM. In the case of the EBSD analysis, a conventional electropolishing using a 33% solution of HNO_3 in methanol (typical for aluminum alloys) was not used to

protect the intermetallic layer between steel and aluminum [1].

3.2.5 Transmission electron microscopy

Transmission electron microscopy (TEM) enables to reveal finer features of the material microstructure. Observation were done on microscopes JEOL JEM 2000F and JEOL JEM 2200 FS both working with accelerating voltage 200 kV.

Bright field (BF) imaging was performed to obtain an information about the microstructure. Conventional selected area diffraction (SAED) helps to reveal the phase composition of the studied region/particle. The microscope is also equipped with a secondary electron detector and could work in scanning mode on thick samples.

Samples from the interfacial region (so called lamellas) were prepared in scanning electron microscope Zeiss Auriga Compact equipped by focus ion beam (FIB). A lamella was cut out from the polished surface perpendicular to the rolling direction (see Figure 3.3). After welding the lamella to a grid using platinum deposition, the TEM sample was thinned to electron transparency. The TEM analysis was carried out in transversal direction.

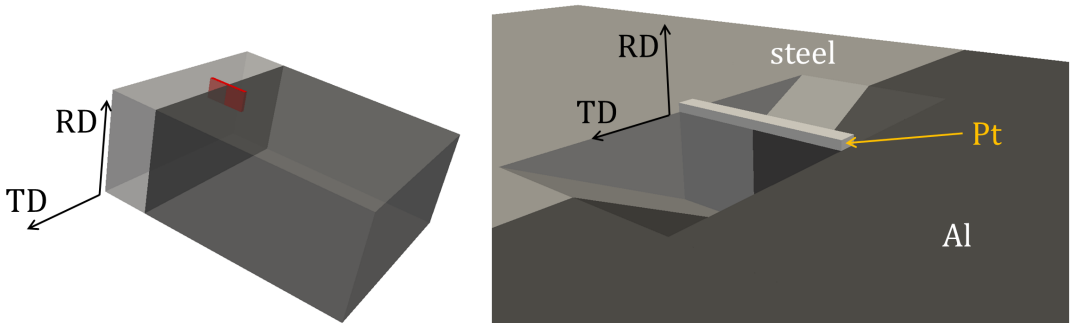

(a) Orientation of the lamella towards transversal and rolling directions.

(b) Scheme of lamella preparation in relation to transversal and rolling directions.

Figure 3.3: Schematic drawings of a lamella preparation.

Moreover, several TEM targets of the aluminum layer were prepared for a study of phase transformations during in-situ annealing in TEM. Slices of the material of initial thickness around 0.5 mm were thinned mechanically on SiC grinding papers up to the thickness of 0.15 mm. Targets of the 3 mm diameter were then punched and electrochemically thinned in Tenupol-5 at –19 °C in the 33% solution of HNO_3 in methanol.

3.2.6 Positron annihilation spectroscopy

A positron source in the form of ^{22}NaCl was sealed between two Mylar and then sandwiched by two identical samples prepared for PAS. An activity of the used source was about 1.3 MBq. A typical coincidence counting rate is 75 s^{-1}.

[1] EBSD analysis of aluminum layer in the as-cast state was performed on a TEM foil after electrochemical thinning using the conventional solution of HNO_3 in methanol due to a finer grain structure requiring better surface quality than annealed samples with coarse grains.

The timing resolution of the employed spectrometer is 150 ps. A detailed description of both positron lifetime (PLS) and coincidence Dopler's broadening (CDB) spectrometer can be found in publications [62] a [63].

For investigation of the as-cast Al-steel clad material several samples with dimensions 1 x 1 cm^2 were prepared. The measurement was performed from Al side and from steel side to make a separate characterization of each layer.

To observe processes connected with diffusional flow during subsequent annealing experiment, samples with the Al-steel interface near the sample surface were prepared. A thickness $\sim$100 μm of Al layer allowing 50 % of positrons pass through was calculated from the empirical relation for the positrons penetration depth [64]

$$P(x) = a_+ e^{-a_+ x}, \tag{3.7}$$

where $\frac{1}{a_+}$ denotes a mean penetration depth which on a maximal kinetic energy E_{max} of the positrons emitted by the source and density of the material ρ

$$\frac{1}{a_+}[cm] \approx \frac{E_{max}^{1,4}[MeV]}{16\rho[g.cm^{-3}]}. \tag{3.8}$$

Samples were then grinded on SiC papers from Al side to thickness between 80 μm and 150 μm. This variance of the thickness was caused by a curvature of the Al-steel clad sheet after the casting.

Results

4.1 Characterization of the as-cast state

4.1.1 Light optical microscopy

The first characterization of the Al-steel clad sheet was done by means of light optical microscope. All micrographs show the plane perpendicular to TD. Overall view through the clad strip is displayed in the Figure 4.1. Analysis by the light optical microscopy was further focused on the phases distribution in the aluminum layer (Figure 4.1 (b)) and the interface region. Colonies of the primary phases were arranged rather in chains orientated in the casting direction on both outer parts of the aluminum layer (Figures 4.2 (a), (c)) whereas in the central part the smaller round particles were randomly distributed. Occasionally, central segregations were present near the center of the strip (see Figure 4.2 (b)). A slight difference of the phase distribution on the opposites edges of the aluminum layer (with and without the adjacent steel substrate) could be also noticed.

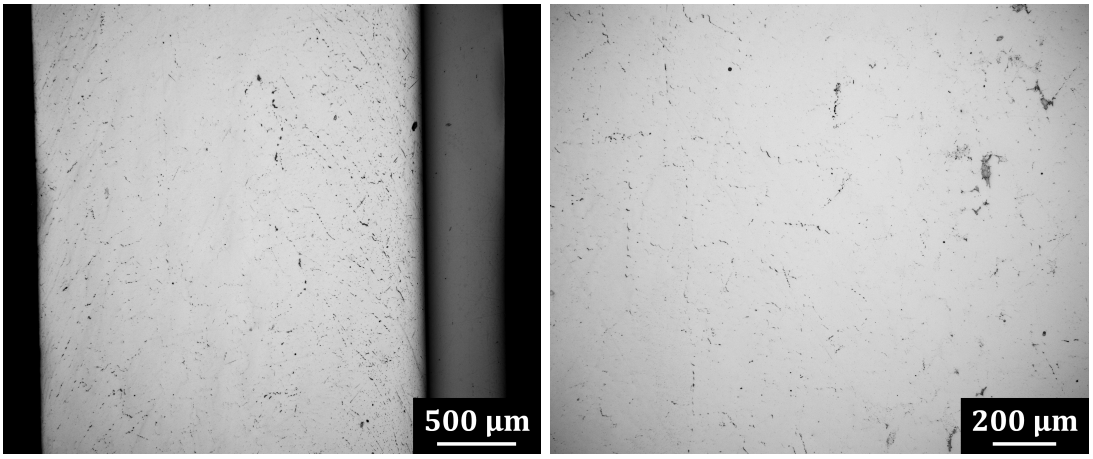

(a) Micrograph through the whole clad strip thickness.

(b) Central part of the aluminum layer showing the phase distribution

Figure 4.1: Microstructural overview of the clad strip.

In the interfacial region, no continuous intermetallic layer was found. Nevertheless, larger density of the primary phases than on the other side of the aluminum layer was observed 4.2 (d). This feature was probably a consequence

of the presence of the steel strip which impeded the heat flux during the casting.

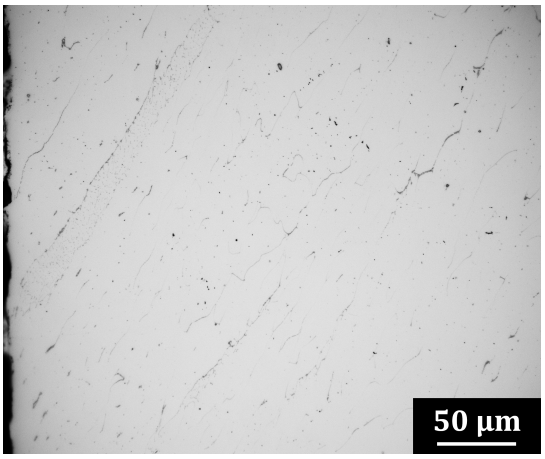

(a) Edge of the aluminum layer without the steel coating.

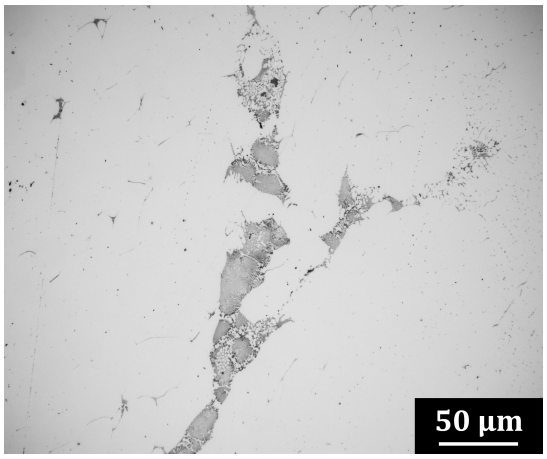

(b) Segregated primary phases near the center of the strip.

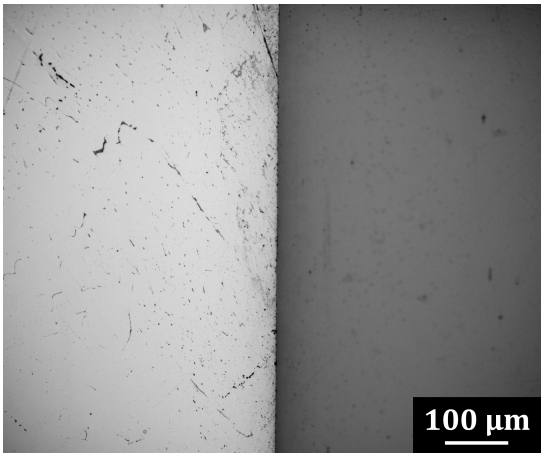

(c) Interfacial region between aluminum and steel layer.

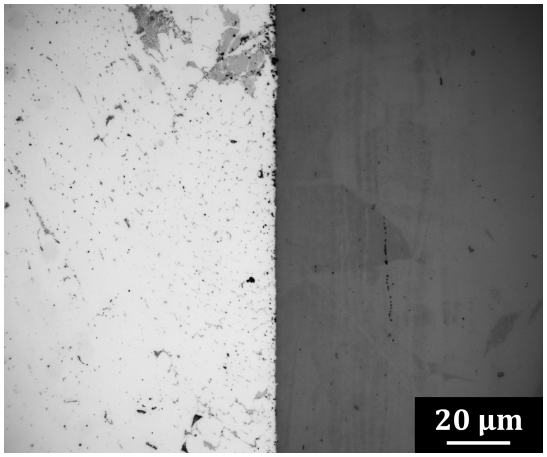

(d) Detail of the interfacial region of the clad strip.

Figure 4.2: Representative parts of the aluminum layer.

4.1.2 Scanning electron microscopy

Grain structure and phase distribution was further studied by scanning electron microscope. In the Figure 4.3, an overview with the aluminum-steel interface is displayed. An equiaxed grain structure through the whole thickness of the steel strip was revealed in the channeling contrast. Moreover, it could be seen that many of the grains contain twins.

Dendritic colonies with eutectic features were found in the aluminum layer near the interface. Some regions containing only smaller particles of the primary phases close to the joint were also present.

Grain structure of the aluminum part of the strip was exposed after electrolytical etching by a solution of nitric acid. Figure 4.4 (a) shows the grain structure

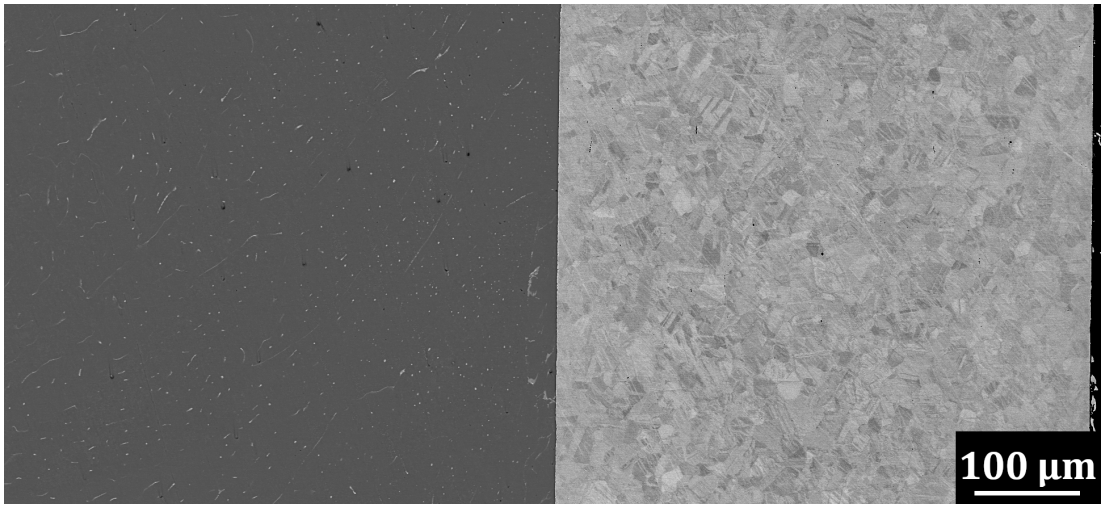

Figure 4.3: Microstructural overview. The whole thickness of the steel layer is depicted.

of the aluminum layer near the edge without the adjacent steel substrate while the Figure 4.4 (a) displays a central part of the aluminum layer. A variance of the phase arrangement through the Al layer was also observed (see Figure 4.5). Primary phases formed linear chains and decorated the grain boundaries of the equiaxed aluminum grains. Towards the central part of the strip, primary phases comprised small dendritic colonies rather than the linear chains or they were present in the aluminum matrix as round particles.

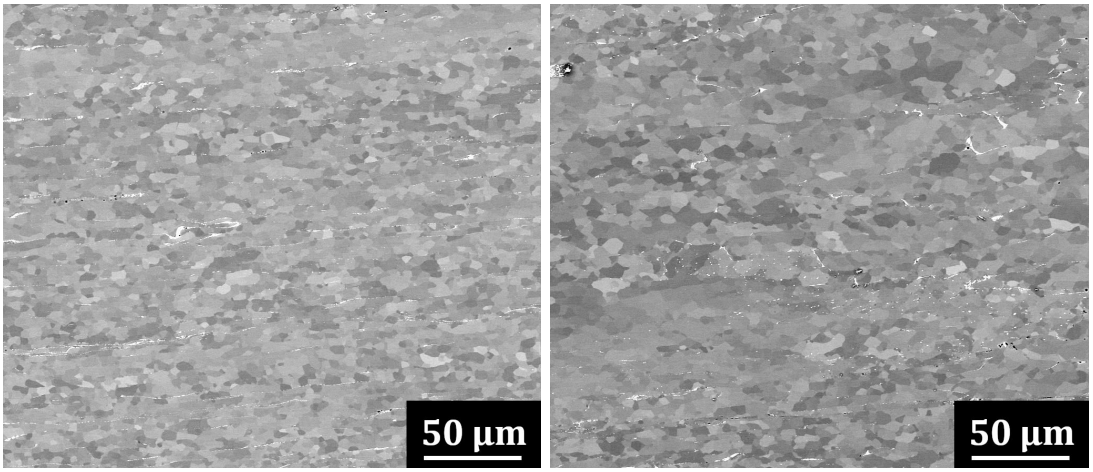

(a) Near the edge region of the Al layer. (b) Central part of the aluminum layer.

Figure 4.4: Grain structure of the aluminum layer.

Study of the aluminum-steel interface did not reveal any continuous layer of the intermetallic phases (see Figures 4.6). Rarely, only a tiny separated isles of the intermetallic phases were found on the aluminum-steel border.

The quantitative analysis of the grain size and orientation were studied by means of electron back-scatter diffraction. Analysis nearly through the whole

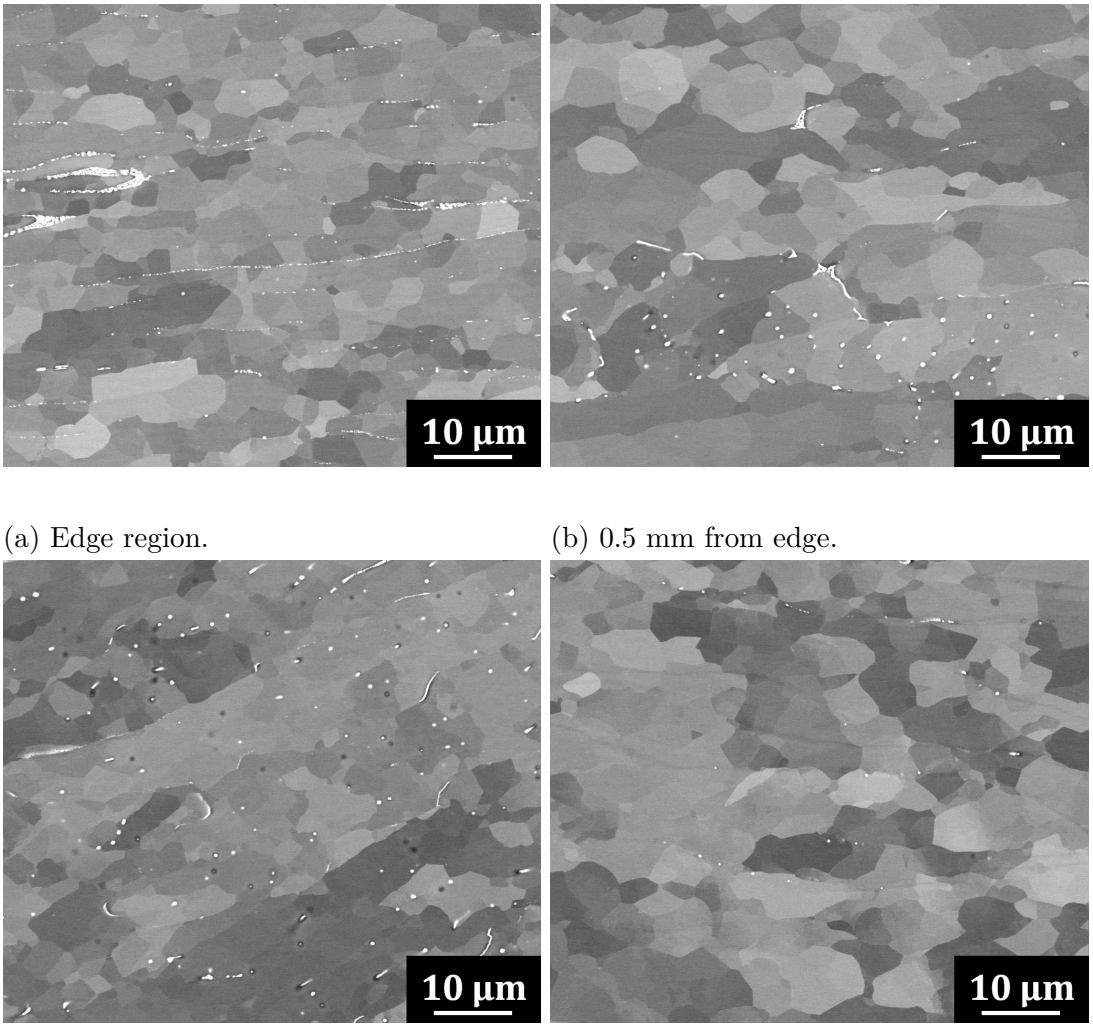

(a) Edge region.

(b) 0.5 mm from edge.

(c) 1 mm from edge.

(d) 1.5 mm from edge (strip center).

Figure 4.5: Grain microstructure of the aluminum layer.

sample thickness was done with two additional detailed scans. Figures 4.7 shows the inverse pole figures of the selected regions in the aluminum layer. Since an inhomogeneous grain size and shape was found, a location of the regions of interest was provided by the left scheme. Magnification used for scans “1” and “2” in the Figure 4.7 circa corresponds with that of the SEM images 4.5.

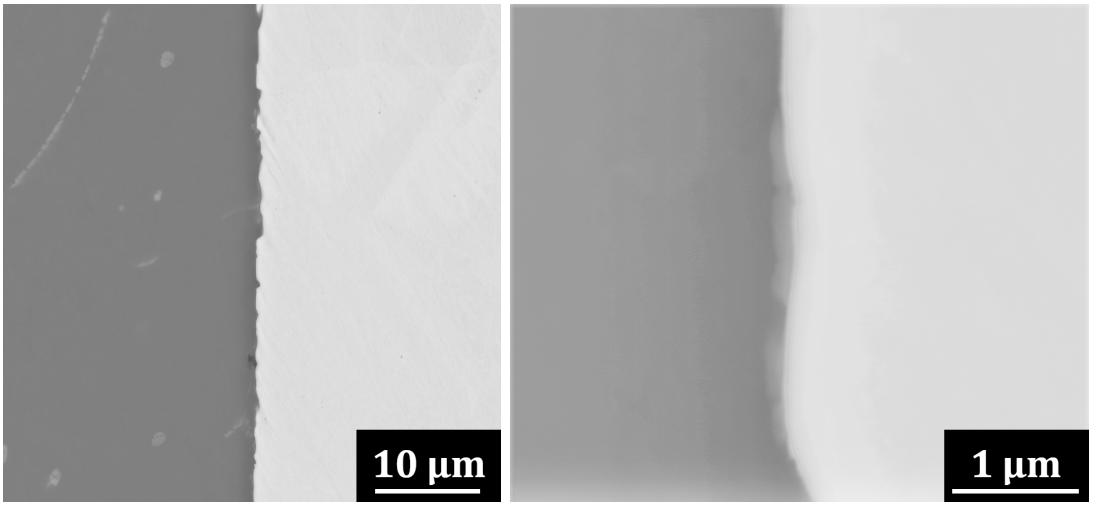

(a) No continuous intermetalic layer. (b) Rare intermetallic particles.

Figure 4.6: Interface region between steel and Al.

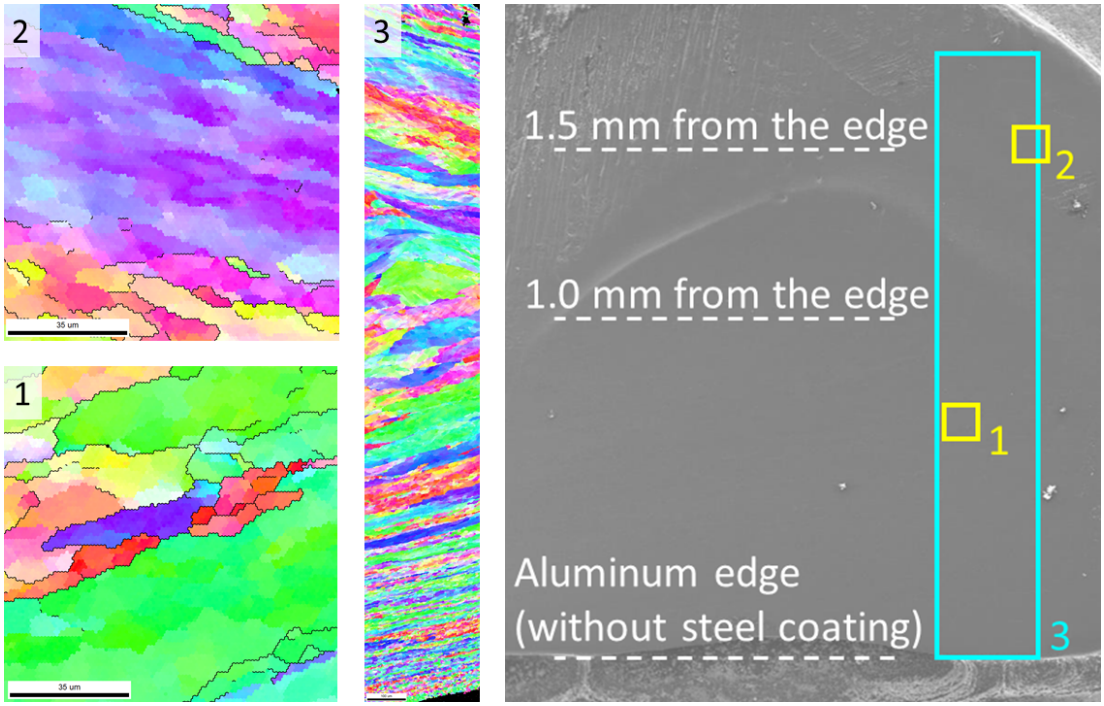

Figure 4.7: Inverse pole figures of the aluminum layer with corresponding location scheme of the scanned regions.

4.1.3 Transmission electron microscopy

Analysis by TEM confirmed that aluminum layer was composed of aluminum matrix and eutectic colonies of the primary particles. These colonies often decorated the grain boundaries (see Figure 4.8) or were surrounded by dislocations. The grains divided into subgrains of average size in the range of several micrometers.

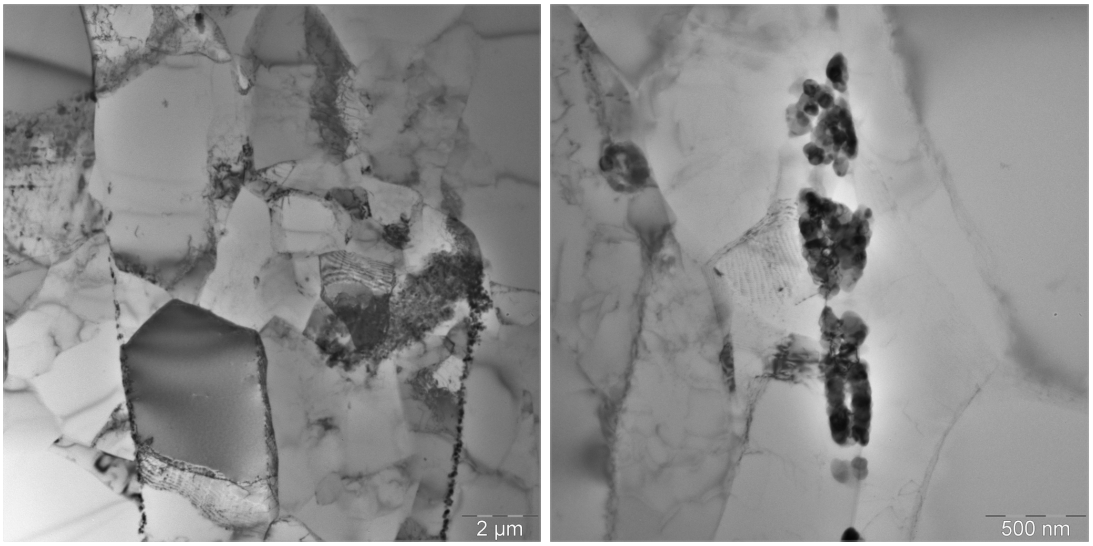

Figure 4.8: Initial microstructure of the as-cast aluminum layer showing dislocation substructure and primary particles decorating (sub)grain boundaries.

The interfacial region is displayed in Figures 4.9. In some places where microscopic grooves in the steel substrate were present, pores were found between aluminum and steel layer.

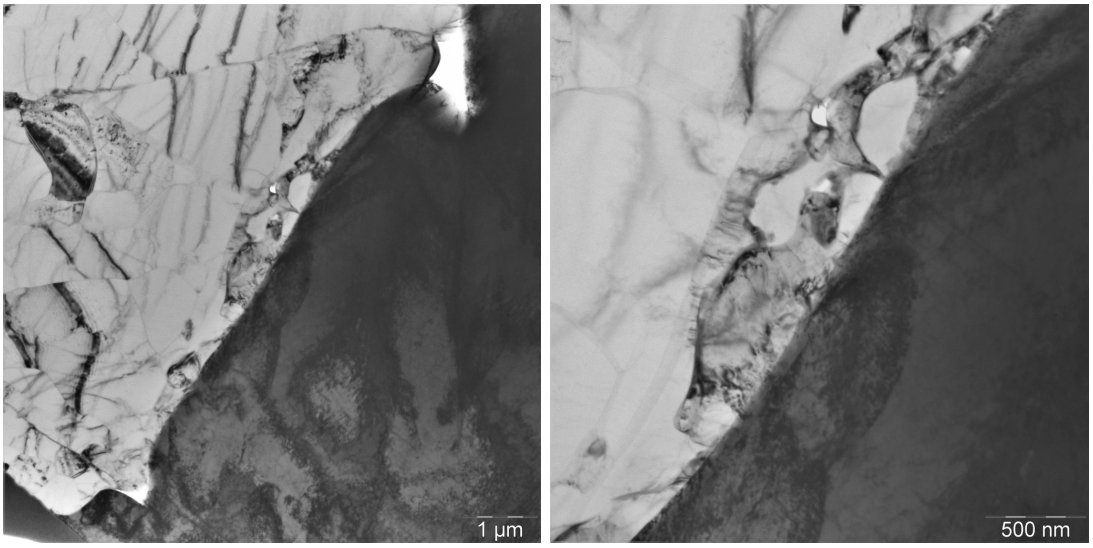

Figure 4.9: Region of the aluminum steel joint.

Nearby the interface, observation of the aluminum and steel microstructure was performed with corresponding micrographs displayed in Figures 4.10. Tiny particles were discovered on the aluminum side. Dislocation tangles were present in both aluminum and steel layer.

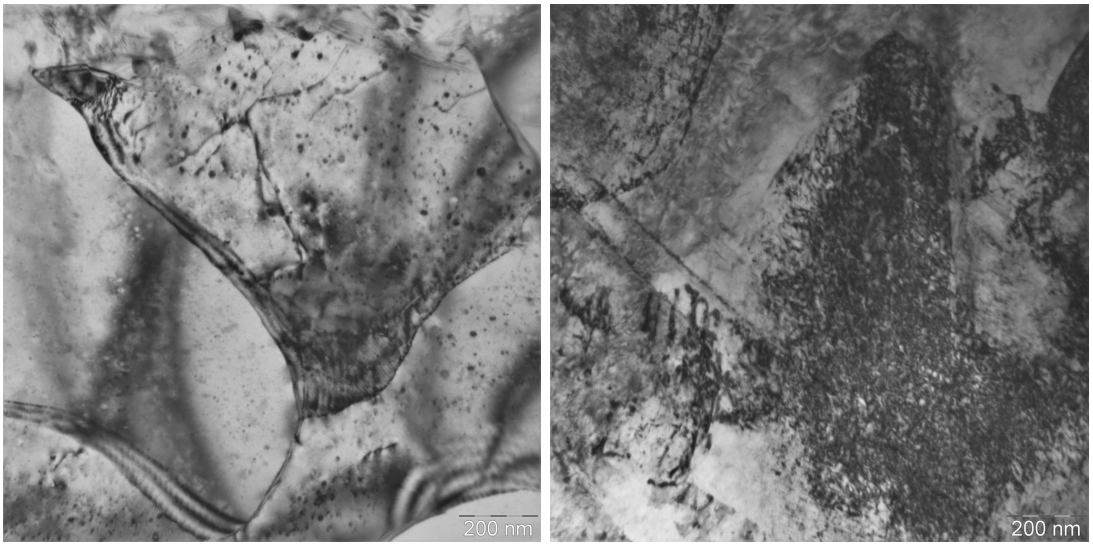

(a) Aluminum side. (b) Steel side.

Figure 4.10: Region of the aluminum steel joint.

4.1.4 Positron annihilation spectroscopy

Positron annihilation spectroscopy was used for evaluation of the material defects. Steel layer, aluminum layer and the region of the joint of the as-cast material were investigated on individual samples which were described in the previous chapter.

Positron life spectroscopy

Both Al and steel layer have two-component PL spectrum. One component reflects the annihilation in a bulk in the delocalized state, the second component is connected to annihilation of positrons trapped on dislocations. Parameters of the exponentials are written in the Table 4.1.

Table 4.1: Measurement of the positron lifetime separately for Al and steel

Sample	τ_1 [ps]	I_1 [%]	τ_2 [ps]	I_2 [%]
Al	(107.8 ± 3.1)	(29.5 ± 1.0)	(230.2 ± 1.1)	(70.5 ± 1.0)
steel	(74.5 ± 2.9)	(41.8 ± 1.5)	(160.9 ± 1.5)	(58.2 ± 1.5)

As the requirements of the simple trapping model (STM) were satisfied, the fit of both PL spectra was fitted also by STM. The parameters are presented in the Table 4.2.

PL spectrum of the sample revealing the interface region do not show any additional components which could be connected with potential voids or pores created during the casting process. The spectrum was properly fitted by four exponential components corresponding to the annihilation of positrons delocalized in Al and steel and positrons trapped in dislocations in Al and steel. The parameters of the exponential components are written in the Table 4.3 and the measured

Table 4.2: Measurement of the parameters τ_B, τ_D, K_D of the simple trapping model separately for Al and steel layer with backwards calculations of parameters τ_1, I_1, τ_2 and I_2 of the exponential components

Sample	τ_B [ps]	τ_D [ps]	k_D [%]	
Al	(165 ± 0)	(226.6 ± 0.6)	(4.6 ± 0.1)	
steel	(107 ± 0)	(160.2 ±0.7)	(4.5 ± 0.1)	
Sample	τ_1 [ps]	I_1 [%]	τ_2 [ps]	I_2 [%]
Al	94.2	26.5	226.6	73.4
steel	72.4	41.0	160.2	59.0

data with the results of decomposition of the PL spectrum accompanied by the weighted residuals of the fit are shown in the Figure 4.11.

Table 4.3: Measurement of the positron lifetime in as-cast Al-steel clad material. $^{22}_{11}$Na positron source was located $\sim$ 140 μm from the Al-steel interface.

Sample	τ_1^{Al} [ps]	I_1^{Al} [%]	τ_2^{Al} [ps]	I_2^{Al} [%]
Al-steel	(123.7 ± 6.7)	(21.9 ± 3.2)	(232.2 ± 1.3)	(62.0 ± 1.6)
	τ_3^{Fe} [ps]	I_3^{Fe} [%]	τ_4^{Fe} [ps]	I_4^{Fe} [%]
	(41.3 ± 3.1)	(11.6 ± 1.2)	(136 +/- 15)	4.5

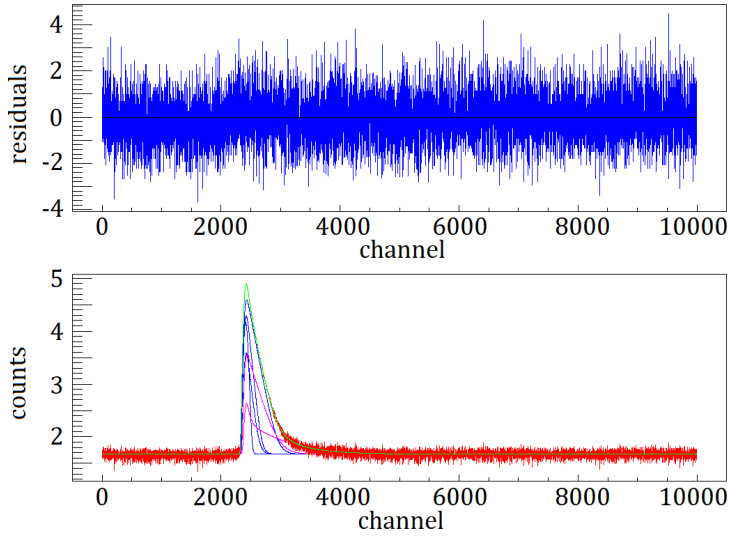

Figure 4.11: Data fitted by four exponential components with the parameters written in the Table 4.3.

Coincidence Doppler broadening spectroscopy

In order to evaluate more precisely the fraction of positron annihilation in Al and in steel in examined samples, CBD spectroscopy was carried out. Momentum distribution of annihilating positron-electron pairs was obtained from the one-dimensional cut of CDB spectrum. The results were compared among all samples by ratio curves related to well annealed aluminum.

As the CDB profile of Fe has wider maximum due to contribution of d-electrons, that Al do not have, a noticeable blue peak appeared in the ratio curve (Figure 4.12) of the sample measured from the steel side. The green data answer to the "experimental" wedge-shape sample prepared by an oblique cut. The positron source was located in such place, that the positrons were supposed to go through both Al and steel layer. Even though, the sample has the most favorable ratio (near 50 %) of annihilation in Al and in steel, it was not suitable for annealing experiment connected with multiple measurement, where the positron source should be located in the "same" place. Furthermore, diffusional processes could be affected due to the character of the cut. Red curve represents too thick Al layer so only 4 % of positrons annihilated in steel. The violet line belongs to the sample described in the PLS part. Square-shaped sample was cut from the Al-steel clad strip and then the Al layer was thinned to the thickness between 80 μm and 150 μm. Only 82 % positrons annihilated in Al and 18 % in steel. The sample was chosen for annealing experiment due to 1) a sufficient ratio of annihilation in Al and steel layer, 2) an ease of positioning of the positron source and 3) almost no influence of the sample geometry on the diffusional processes on the Al-steel interface which, are expected to occur during annealing experiment.

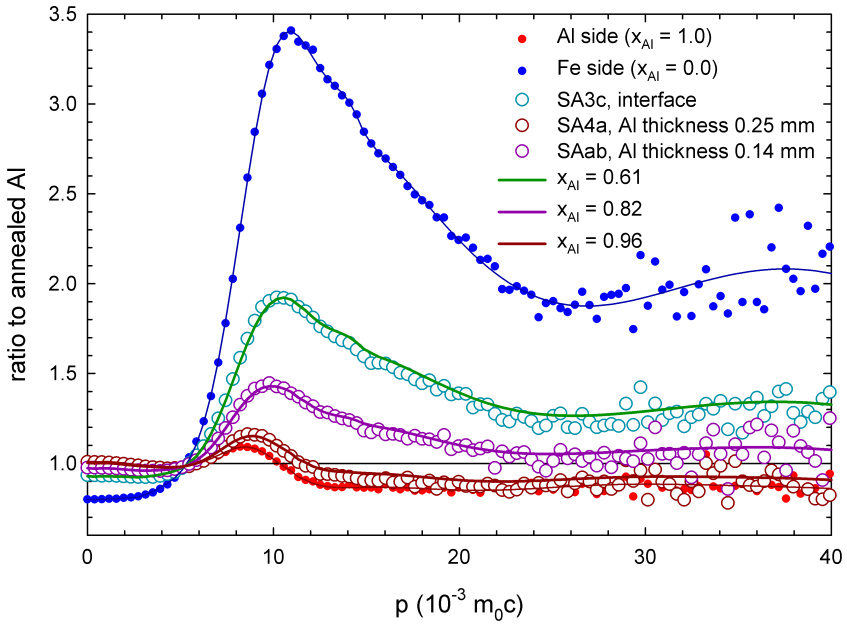

Figure 4.12: CDB ratio curves

4.2 Isochronal heat treatment

4.2.1 Electrical resistivity

First and foremost, electrical resistometry was carried out between the individual steps of isochronal annealing to monitor the microstructural changes. Figure 4.13 shows the electrical resistivity annealing curves $\frac{\rho(T)-\rho_0}{\rho_0}$, where ρ_0 denotes the resistivity before the annealing experiment. Corresponding resistivity annealing spectra $-\frac{1}{\rho_0}\frac{\partial\rho}{\partial T}$ are displayed in the Figure 4.14. Almost no changes were observed in the steel sample. Similar course of aluminum and composite resistivity curves were detected, since the transformations occurring in aluminum layer had a main influence on resistivity. Nevertheless, a slight difference was revealed in the annealing spectra. Aluminum sample exhibited two local maxima situated bellow 250 °C and 400 °C whereas the one close to 250 °C was partially suppressed in the sample of the composite.

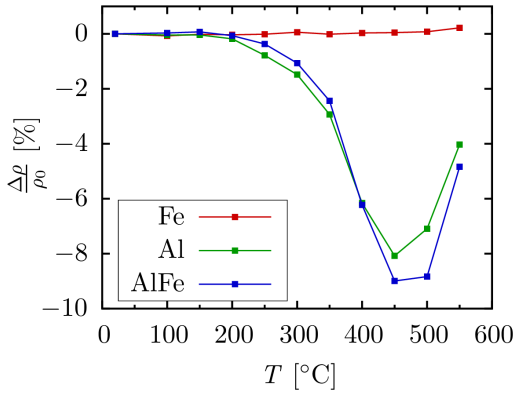

Figure 4.13: Relative changes of electrical resistivity during step-by-step annealing

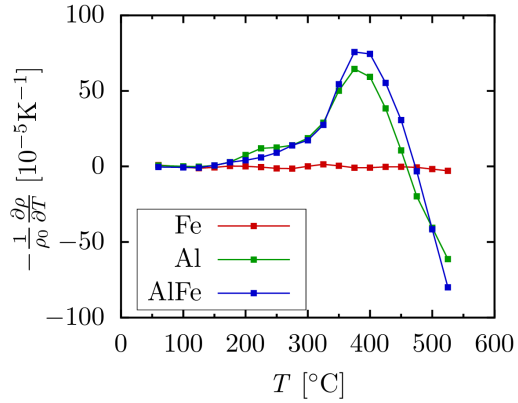

Figure 4.14: Resistivity annealing spectra calculated from resistivity data.

Figure 4.15 displays the evolution of RRR values during the isochronal annealing. Up to 300 °C, no changes were observed in all samples. Then, an abrupt

increase of RRR occurs for aluminum and clad sample above 350 °C. Between 450 °C and 550 °C, a pronounced decrease followed in these samples. Displayed error bars were evaluated from a possible temperature uncertainty of 2 °C introduced from measurements in ethanol.

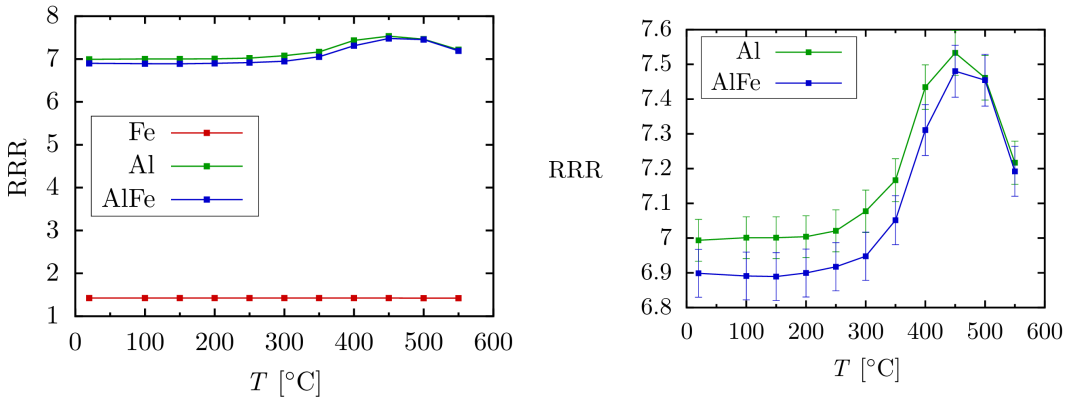

Figure 4.15: Residual resistivity ratio during step-by-step annealing.

4.2.2 Light optical microscopy

Microstructural changes during the heat treatment were investigated firstly by light optical microscopy. Evolution of the phase distribution in aluminum layer and in the interfacial region can be seen in Figures 4.16 and 4.17. Between 300 °C and 450 °C, a slight coarsening of the phases could be noticed. Further increase of annealing temperatures caused a partial dissolution of the primary particles. Higher magnifications revealed also "new" needle-shape particles after annealing at 600 °C (see the last image of the Figure sequence 4.17).

A formation of the expected intermetallic layer was postponed to higher temperatures. Actually, no intermetallic layer was observed even after annealing at 500 °C. Nevertheless, subsequent annealing step at 550 °C / 25 min caused a significant growth of the interfacial phase. The last heating step at 600 °C resulted in a destruction of the clad sample.

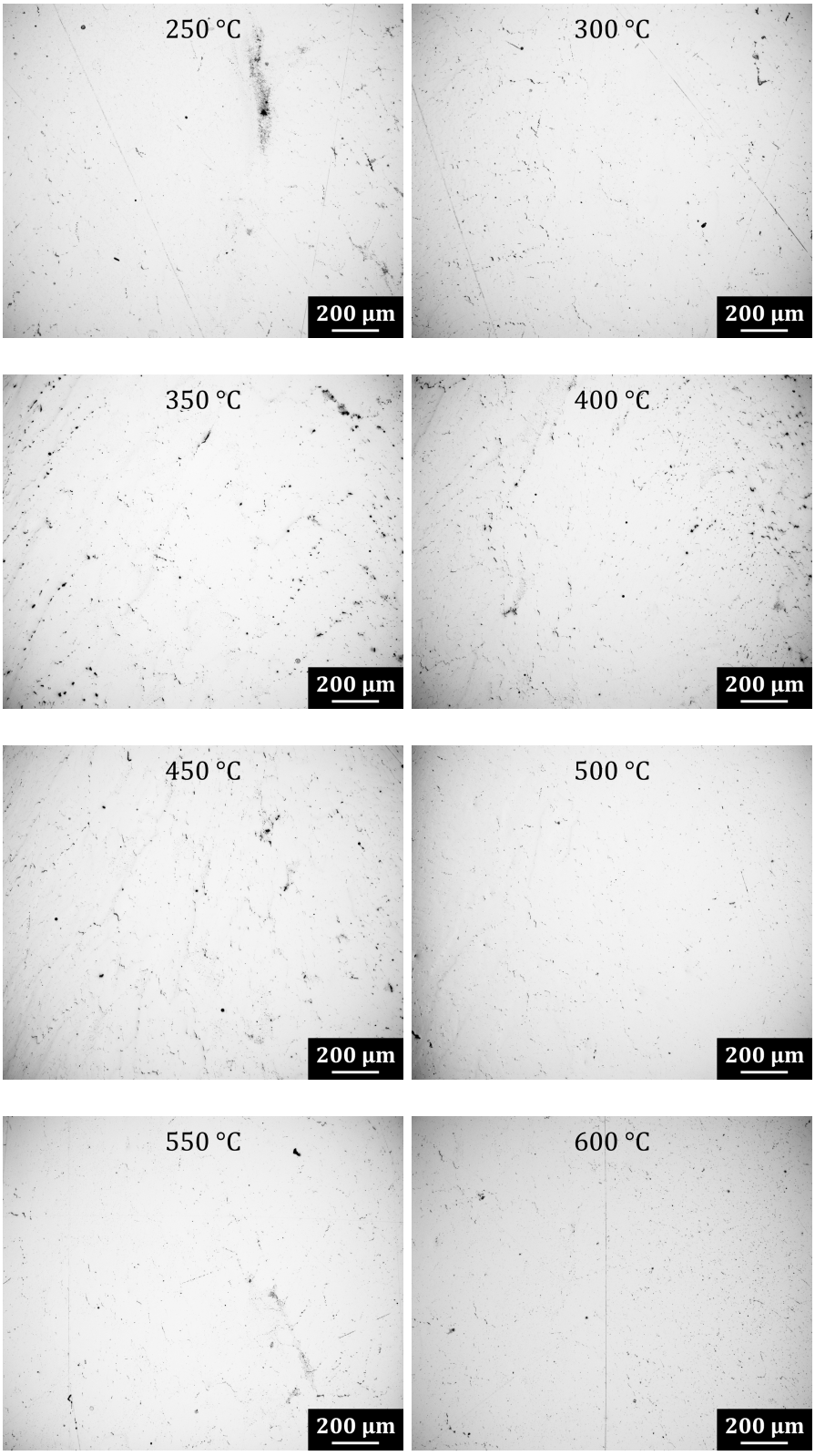

Figure 4.16: LOM images of the microstructural evolution in the central part of the Al layer during isochronal annealing.

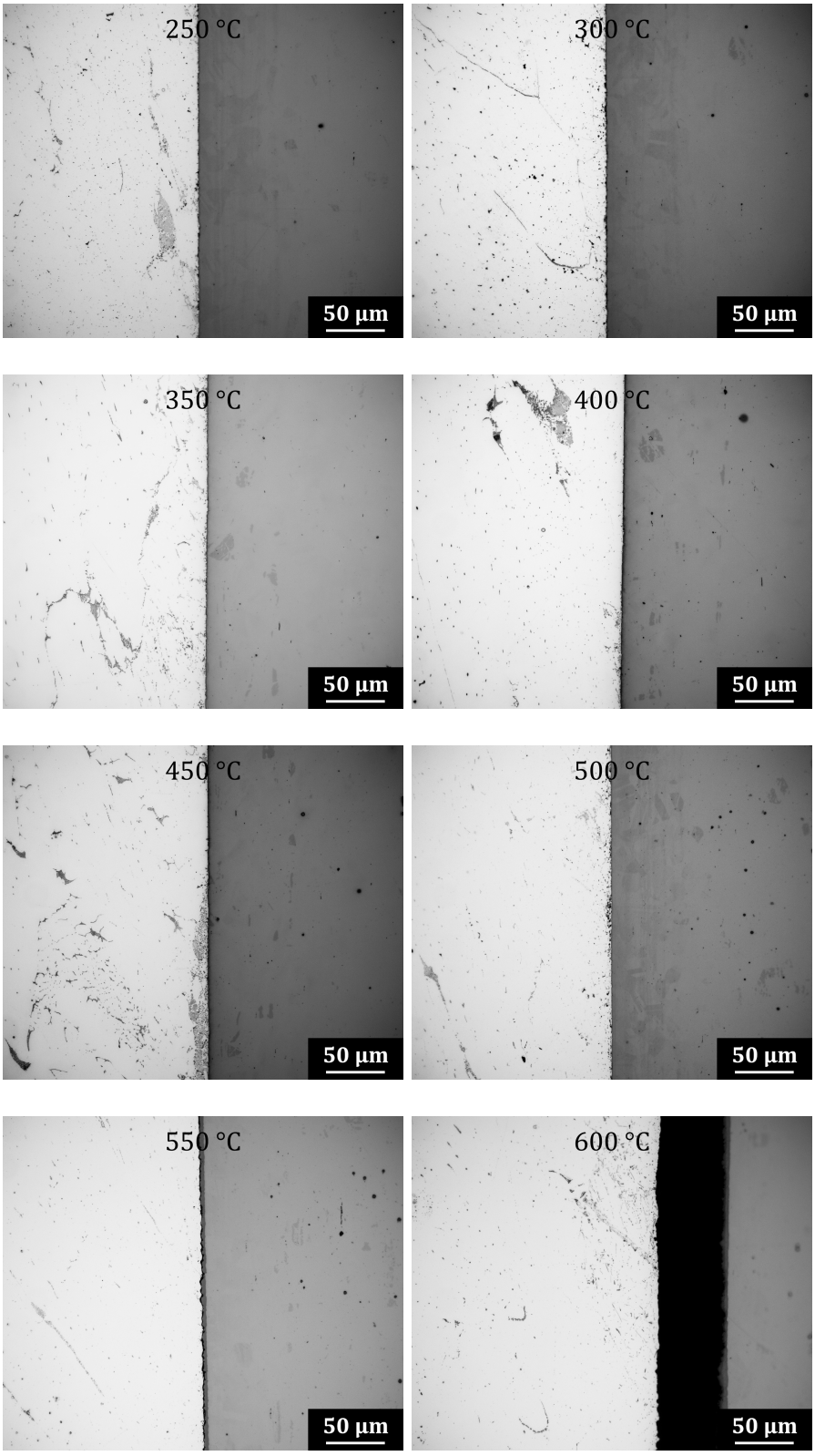

Figure 4.17: Phase distribution near the Al - steel interface.

4.2.3 Scanning electron microscopy

Further analysis of the microstructure with focus on the interface region was done using scanning electron microscope. BSE imaging helped to reveal the phase and grain structure, EDS was used for the determination of the chemical composition of the interfacial region and EBSD was employed to evaluate the grain size and orientation and phase analysis of the interfacial layer.

Evolution of the interfacial phase growth is shown by Figures 4.18 and 4.19. After annealing up to 500 °C, a thin and discontinuous layer of intermetallic phases was observed. Following annealing step then caused a pronounced increase of the layer thickness.

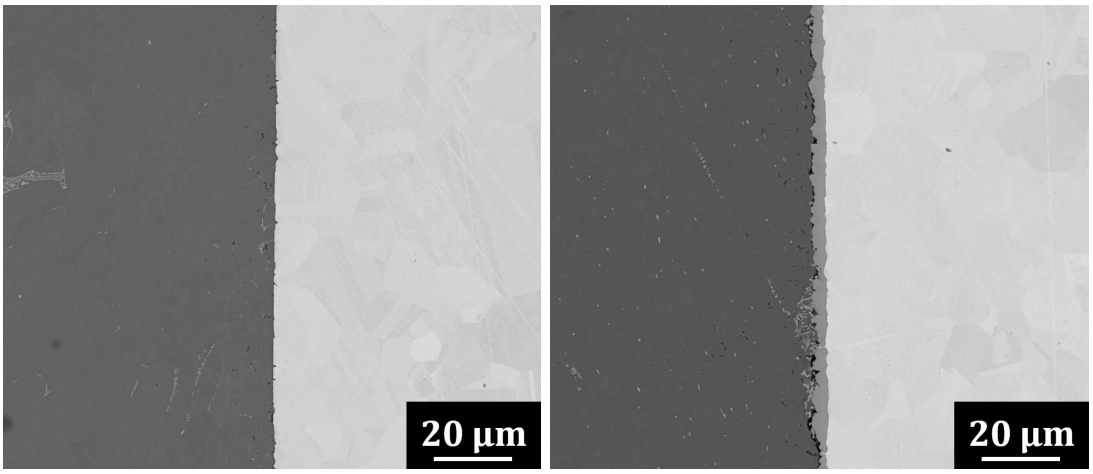

(a) 500 °C (b) 550 °C

Figure 4.18: Microstructural changes during isochronal annealing.

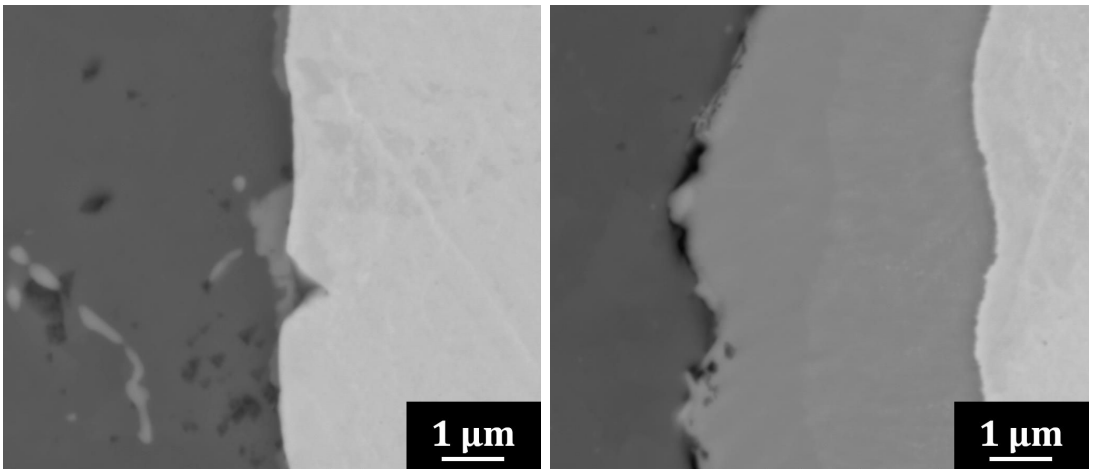

(a) 500 °C (b) 550 °C

Figure 4.19: Detail of the interfacial intermetallic growed during isochronal annealing.

EDX line analysis of the concentration profile was carried out across the interface. States annealed up to 500 °C and 550 °C were studied. Even though, the image contrast obtained by BSE shows several layers varying in brightness which could indicate a different chemical composition, line analysis performed by EDS did not prove it, since no abrupt jump in concentration was measured.

Point analysis was carried out in the region of the phase. The resulting chemical composition is displayed in the Table 4.4.

Table 4.4: Chemical composition (in at.%) of the intermetallic phase obtained by EDS

	Al	Fe	Si	Ni	Cr
500 °C	71.9	19.5	3.5	2.0	3.2
550 °C (near Al)	68.2	21.4	0.7	3.4	6.3
550 °C (near SS)	64.2	23.4	0	4.7	7.7

Electron backscatter diffraction was applied for grain size and orientation evaluation. Figure 4.20 shows recrystallization and coarsening of the aluminum grains as a consequence of heat treatment. Steel strip microstructure remained almost unchanged during whole heat treatment. Inverse pole image of the steel strip after annealing up to 550 °C is displayed in Figure 4.21 and it could be compared with Figure 4.3 which shows the channeling contrast of initial steel grain structure.

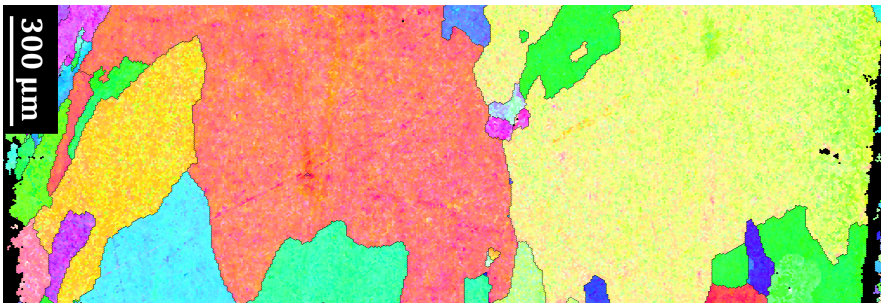

(a) 500 °C

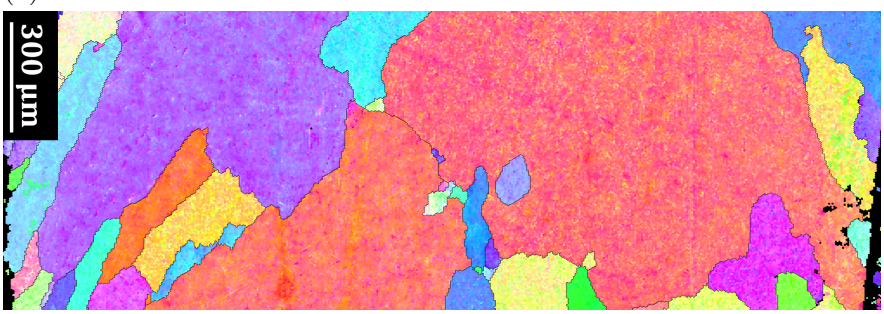

(b) 550 °C

Figure 4.20: Inverse pole figures of Al layer in TD after isothermal annealing

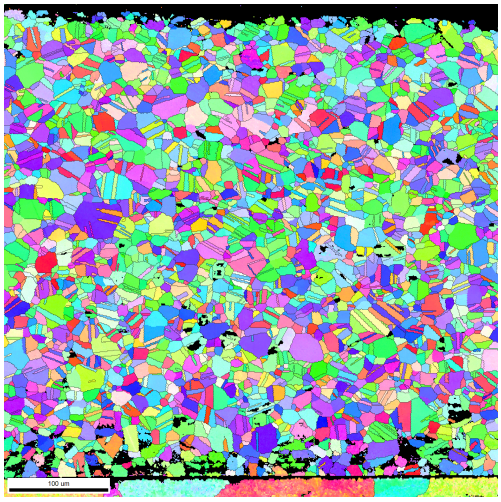

Figure 4.21: Inverse pole figure of steel layer in TD after isothermal annealing up to 500 °C

Figure 4.22 shows inverse pole images of the interfacial layer. Although the quality of the evaluation was not so high, four phases were clearly identified: fcc Al, orthorhombic $Al_{13}Fe_4$, orthorhombic Al_5Fe_2, and fcc steel.

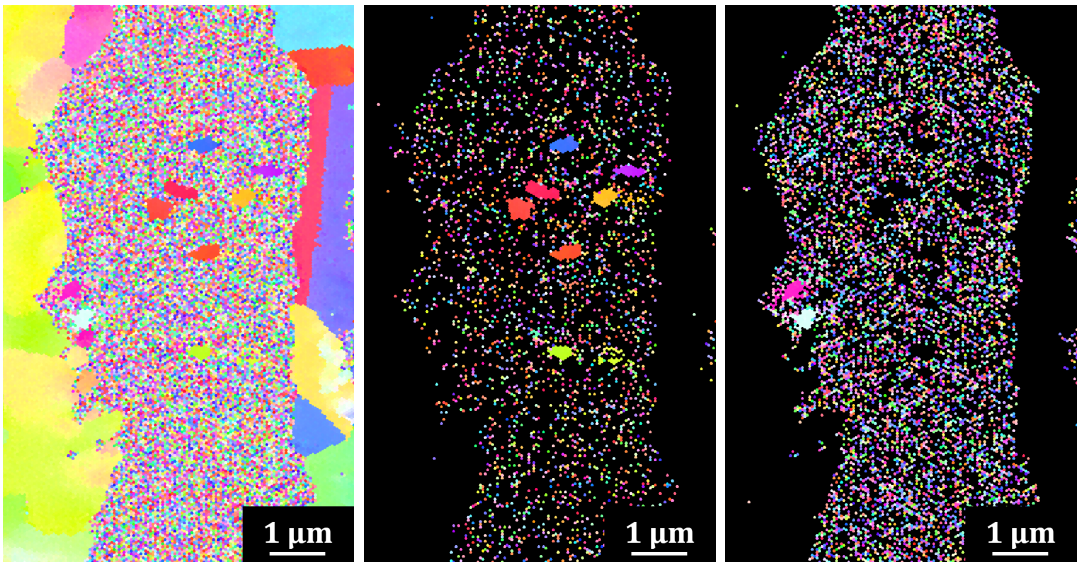

(a) Al - phase - Fe (b) Al_5Fe_2 (c) $Al_{13}Fe_4$

Figure 4.22: Inverse pole figures of intermetallic layer between Al and steel after isochronal annealing up to 550 °C

4.2.4 Transmission electron microscopy

According to isochronal heating scheme applied for resistivity measurement and LOM and SEM observations, an aluminum target was annealed in-situ in TEM for direct observation of the phase transformations. Images of selected states are displayed in Figures 4.23.

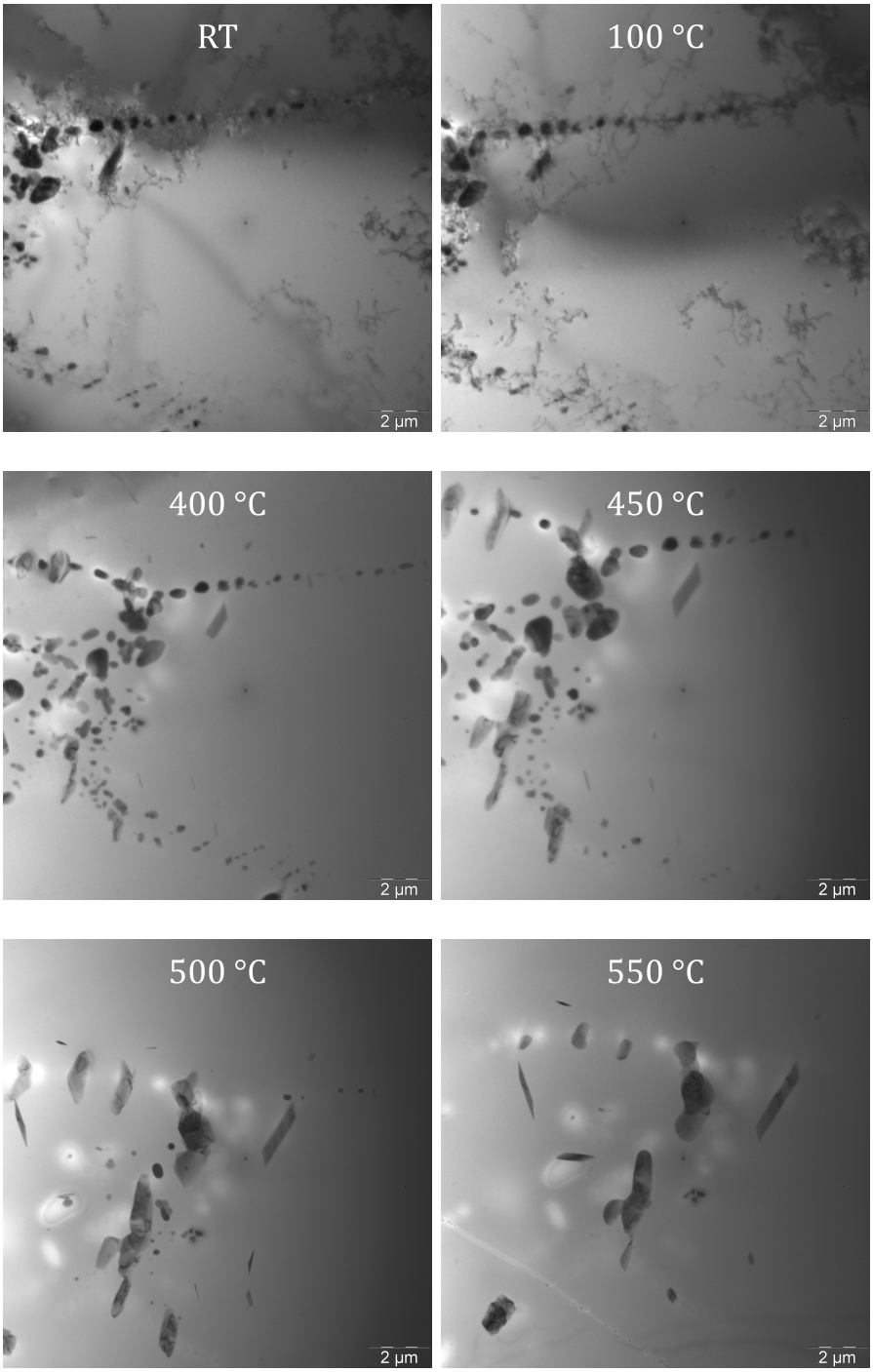

Figure 4.23: In-situ annealing in TEM.

Firstly, dislocation recovery started at low annealing temperatures ranging from 150 °C to 300 °C. Almost no dislocations were observed after annealing up to 450 °C. From these temperatures, also the partial dissolution or transformation of some primary particles became evident.

Diffusional processes on the aluminum-steel interface were monitored during in-situ annealing by SEM in TEM by secondary electrons. No interfacial changes were observed during annealing up to 480 °C. At 500 °C an intensive growth of

intermetallic layer towards steel was observed. Figures 4.24 shows selected states of the in-situ annealing of the interface region.

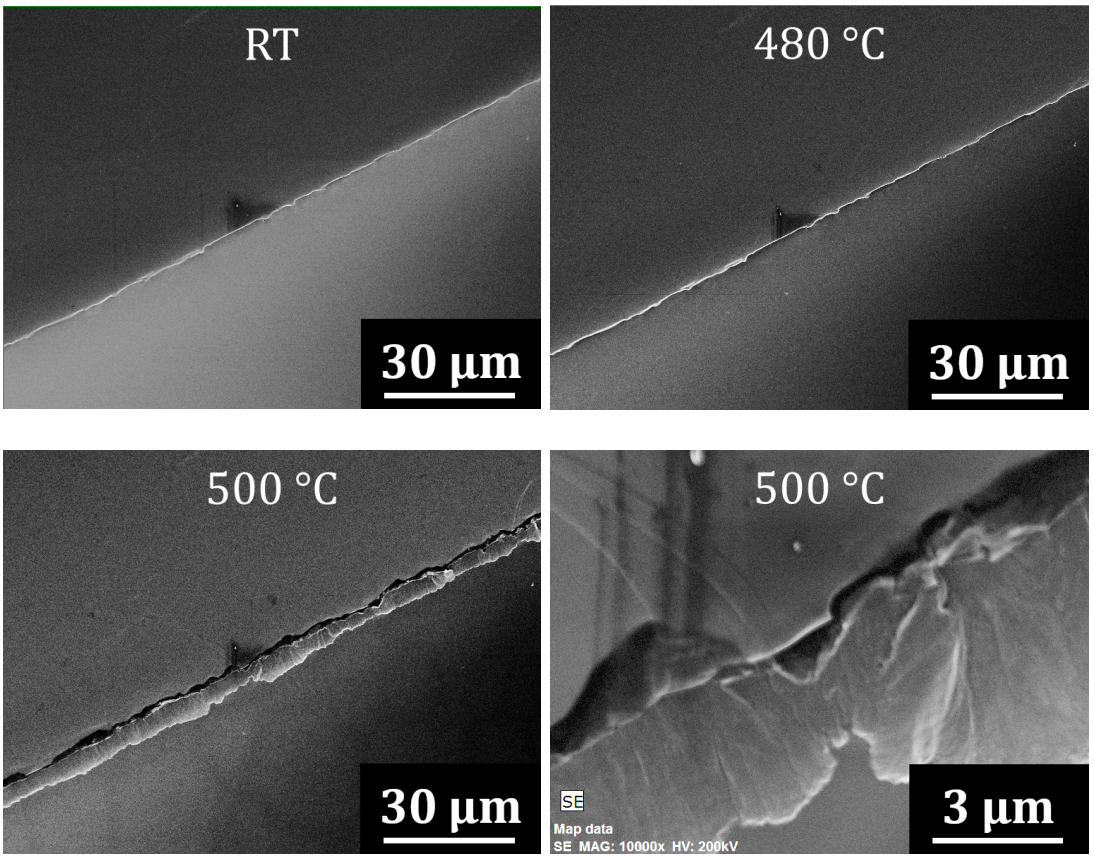

Figure 4.24: In-situ annealing in SEM.

4.3 Isothermal heat treatment

Studied clad material was subjected also to the isothermal annealing at 450 °C and 500 °C. Similar investigation as for isochronal annealing were carried out.

4.3.1 Electrical resistivity

Relative changes of the electrical resistivity were displayed in Figures 4.25. Almost no changes in the case of steel layer. Concerning RRR curves of steel (see Figure 4.26 (a)), much higher value of the experimental error than the observed RRR decrease was introduced by a possible variation of the temperature during the resistance measurements at RT. The maximal temperature uncertainty was estimated as 2 °C which was used for determination of the vertical errorbars displayed in the RRR graphs.

Evolution of $\Delta R/R_0$ of the clad and aluminum sample (Figure 4.25) seems to follow the trends occurred during isochronal annealing with only an accelerated decrease from the beginning of the annealing experiment due to the higher

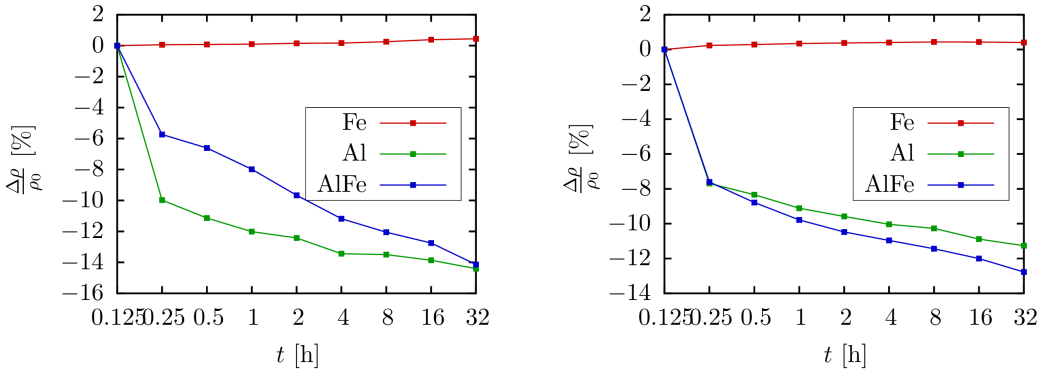

(a) 450 °C (b) 500 °C

Figure 4.25: Relative changes of the electrical resistivity.

temperatures. *RRR* course was evidently increasing and it was related mainly with the phase transformations in the Al layer (Figure 4.26 (b)). Error bars were evaluated from the same temperature uncertainty of 2 °C introduced from measurements in ethanol. Position of the *RRR* curve of the composite between those of Al and steel was in agreement with expectations since *RRR* acts as a conductivity - steel layer in the clad sample is expected to have a decreasing effect on the conductivity of the Al layer.

4.3.2 Scanning electron microscopy

Structural changes mainly of the intermediate layer of the clad material were studied by SEM. During annealing at 450 °C, no intermetallic layer grew on the interface (see Figure 4.27). Evolution of the phase growth during isothermal annealing at 500 °C is displayed in Figures 4.28.

Similarly as in the case of the thick intermetallic layer formed after isothermal annealing at high temperatures, cracking appeared on the "boundary" between aluminum and intermetallic layer.

EDS line analysis of the concentration profile was carried out across the interface. States annealed at 500 °C for 4h, 8 h, 16 h and 32 h were investigated. Several analysis were performed in the case of 4h- and 8h-annealed samples due to uneven formation of intermetallic layer. Atomic concentrations as functions of distance from a point of 50 at.% Al-concentration are displayed by graphs in Figures 4.29. Corresponding BSE-images where the analysis was performed are shown in Figures 4.30. Slightly rised Si-concentration was measured in the interfacial phase near Al. As the Si content is low in comparison with remaining elements, Si concentration was scaled by right y-axes which was added for better resolution.

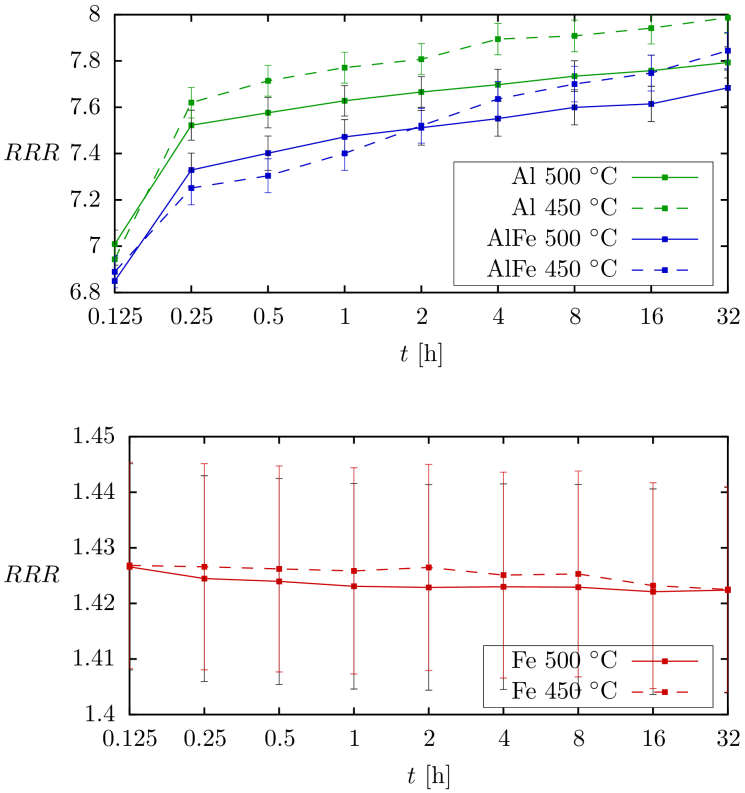

Figure 4.26: Residual resistivity ratio during isothermal annealing

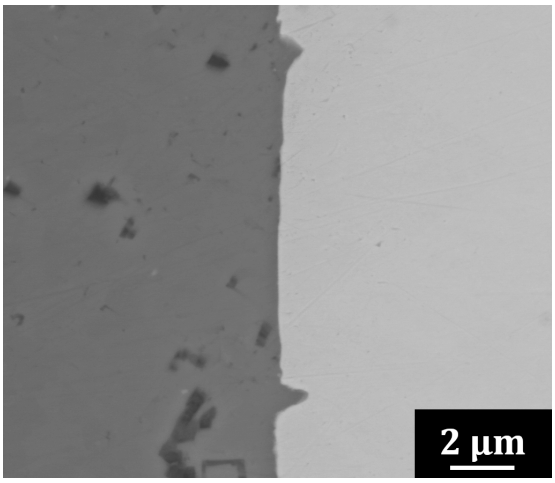

Figure 4.27: SEM image of Al-steel interface after annealing 450 °C / 32 h

4.3.3 Transmission electron microscopy

A detailed characterization of the interfacial layer was done on a TEM lamella, which was prepared from a sample isothermally annealed at 500 °C / 16 h, where the phase was "well developed" and the delamination did not proceed so far. STEM image through the layer thickness is displayed in the Figure 4.31. A twin was found in the steel. The intermediate layer consisted of at least three

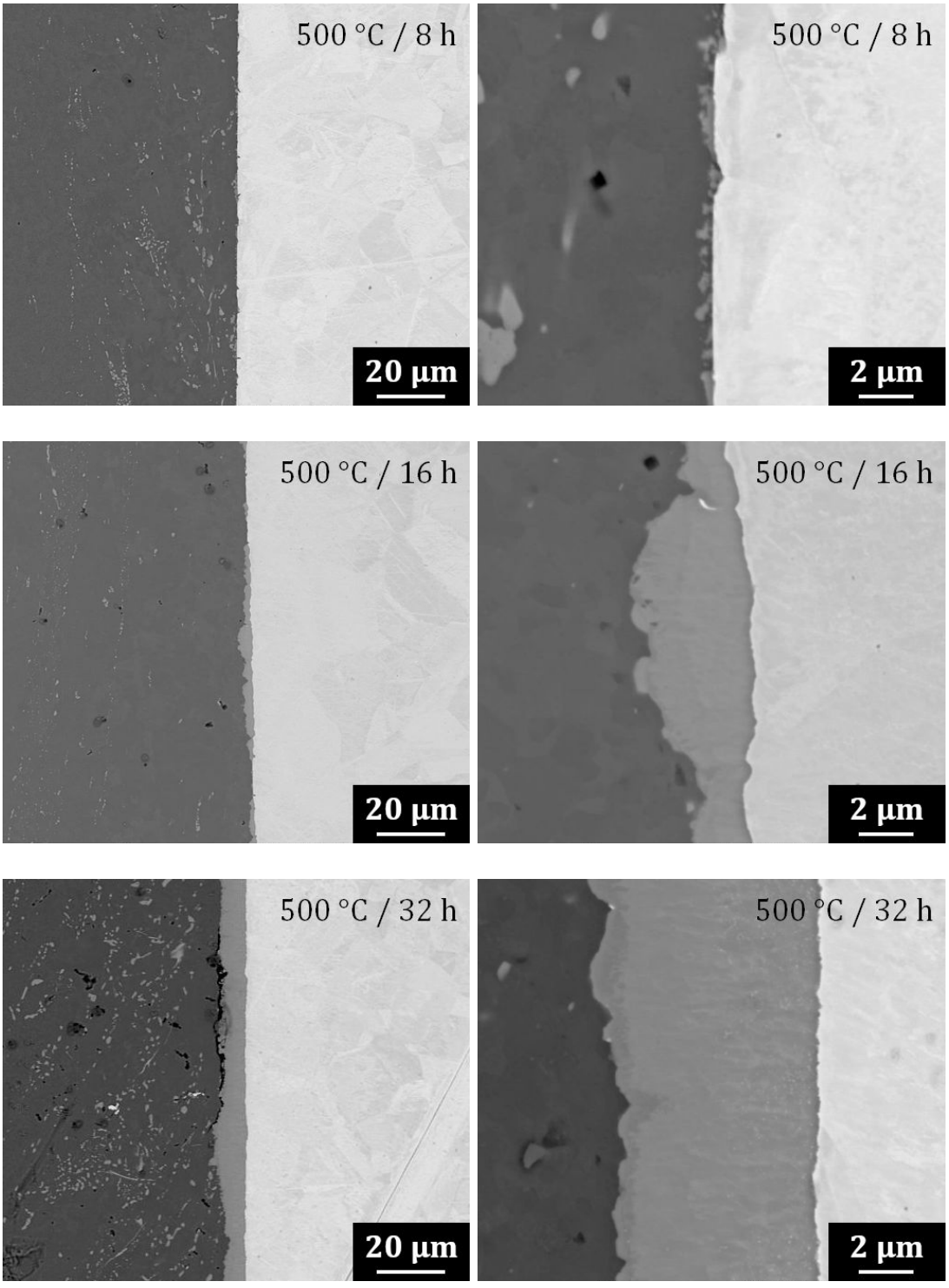

Figure 4.28: SEM images showing evolution of the interfacial phase during isothermal annealing at 500 °C.

sublayers: a sublayer adjacent to the steel contained fine grains elongated in a direction of concentration gradient toward aluminum side. In the following layer, the microstructure changed into long columnar grain preserving the direction of elongation. The third sub-layer close to aluminum side was very thin with

microstructure no longer elongated in the main direction of the diffusional flux but rather in RD.

EDS point analysis was done in places highlighted by yellow squares in the Figure 4.31. Results are displayed in the Table 4.5.

Table 4.5: Chemical composition (in at.%) of the intermetallic phase obtained by EDS

region		Al	Fe	Si	Ni	Cr
1	aluminum	99.2	0.5	0.1	0.04	0.18
2	thin layer	77.1	14.9	5.2	0.15	2.7
3	columnar	75.5	16.4	1.5	1.9	4.7
4	columnar	72.3	16.9	3.6	2.5	4.8
5	fine grains	73.0	18.5	1.2	2.0	5.3
6	fine grains	70.7	20.7	0.18	2.4	6.1
7	steel	0.7	70.4	0.8	8.1	20.1

Distribution of alloying elements or impurities was revealed by EDS map analysis. Ni-rich regions were observed in the intermetallic layer and even in aluminum. Increased concentration of Si was detected in the intermetallic layer close to aluminum. Moreover, an oxidic layer was found between aluminum and the intermediate layer decorating the crack. EDS maps are shown in the Figure 4.32. The concentration profile across the interface was evaluated with and without O-content and the graph is displayed in Figure 4.33.

Selected area electron diffraction patterns were collected together with corresponding bright field image from several regions (see Figures 4.34 and 4.35). The distance between lattice planes and angles were measured and compared with those values provided by Pearson's crystallographic database.

The diffraction pattern taken from an aluminum grain responded to zone [1 0 -1]. Analysis of the steel's diffractogram showed satellite spots that indicates a presence of a twin in the region of interest. In the interfacial layers, "ring diffractograms" were studied. The sublayer containing fine grains was identified as an orthorhombic Al_5Fe_2 phase. Analysis of the columnar-grain layer diffractogram was not unambiguous so it probably consists of several different phases.

Close to aluminum layer, a SAED pattern was obtained from a small particle (see Figure 4.36). Angles and d-spacing were measured: $/phi = 94{,}13$ř, $d_1 = 0{,}850$ nm , $d_2 = 0{,}437$ nm. Identification of the phase was not achieved for the time being.

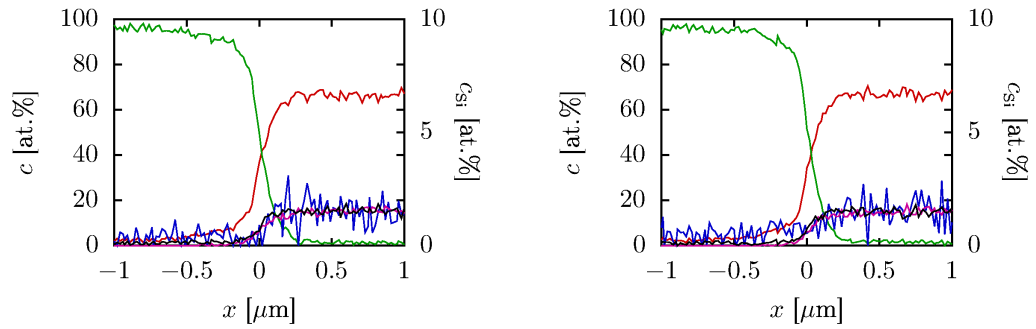

(a) Line A, 500 °C / 4 h.

(b) Line D, 500 °C / 8 h.

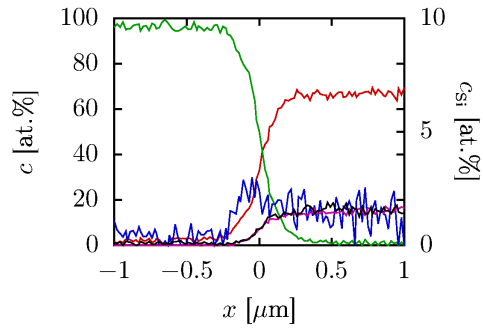

(c) Line B, 500 °C / 4 h.

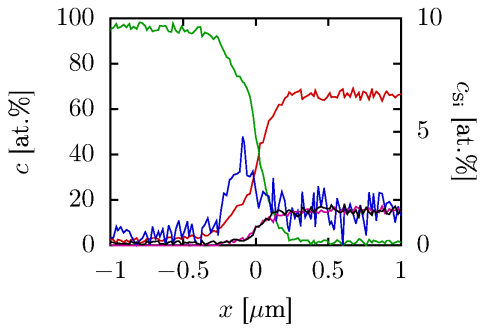

(d) Line E, 500 °C / 8 h.

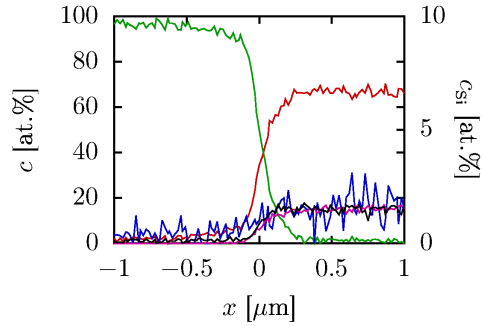

(e) Line C, 500 °C / 4 h.

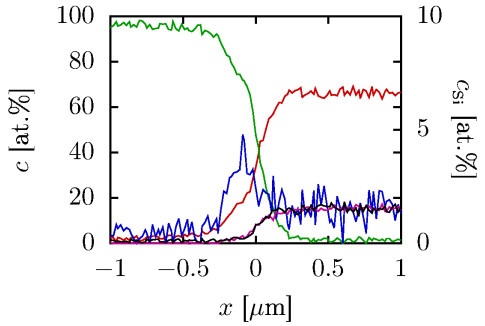

(f) Line F, 500 °C / 8 h.

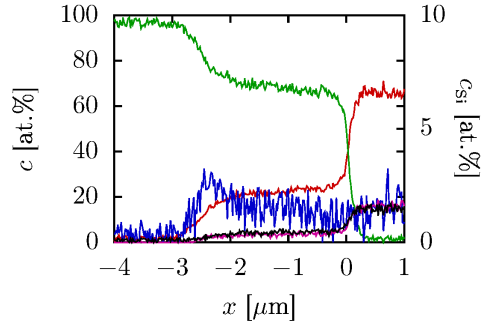

(g) Line G, 500 °C / 16 h.

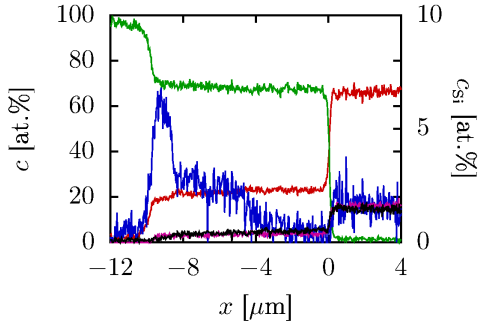

(h) Line H, 500 °C / 32 h.

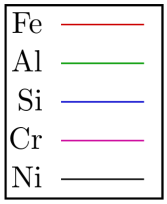

(i) Legend.

Figure 4.29: EDS line analysis of the Al-steel interface after isothermal annealing.

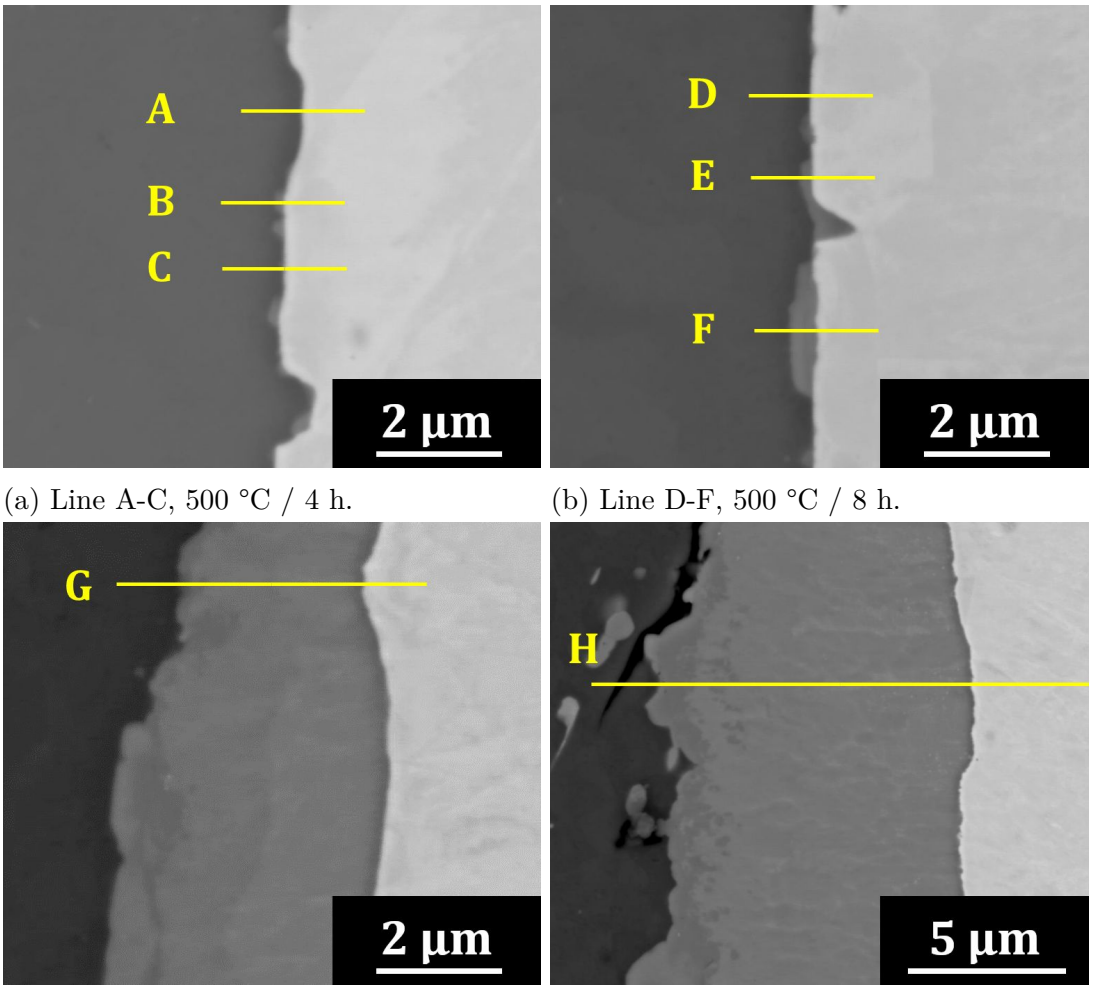

(a) Line A-C, 500 °C / 4 h.

(b) Line D-F, 500 °C / 8 h.

(c) Line G, 500 °C / 16 h.

(d) Line H, 500 °C / 32 h.

Figure 4.30: BSE images of regions where EDS line analyses were performed (see Figure 4.29).

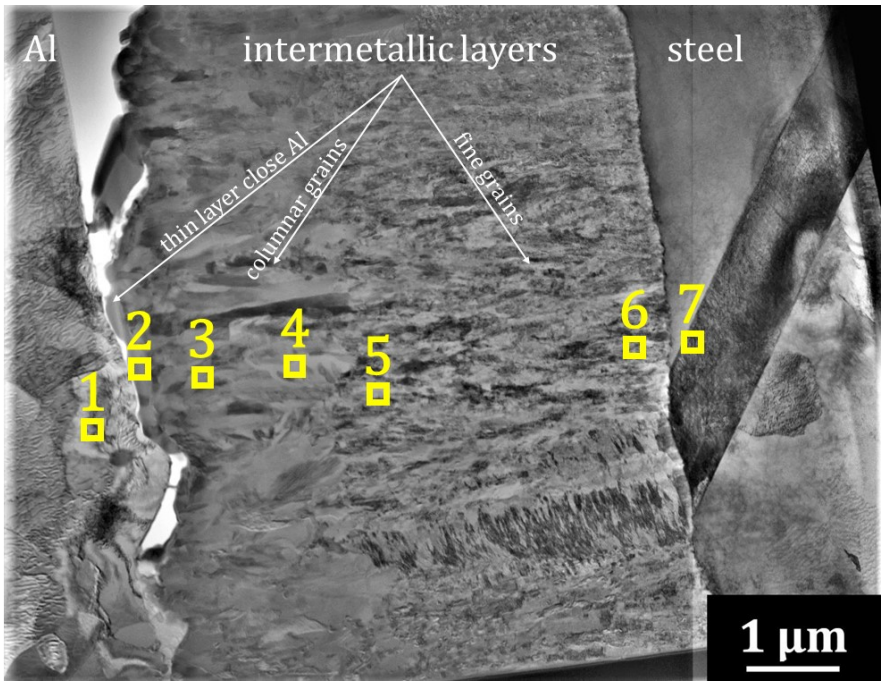

Figure 4.31: STEM image of Al-steel interface after annealing at 500 °C / 16 h

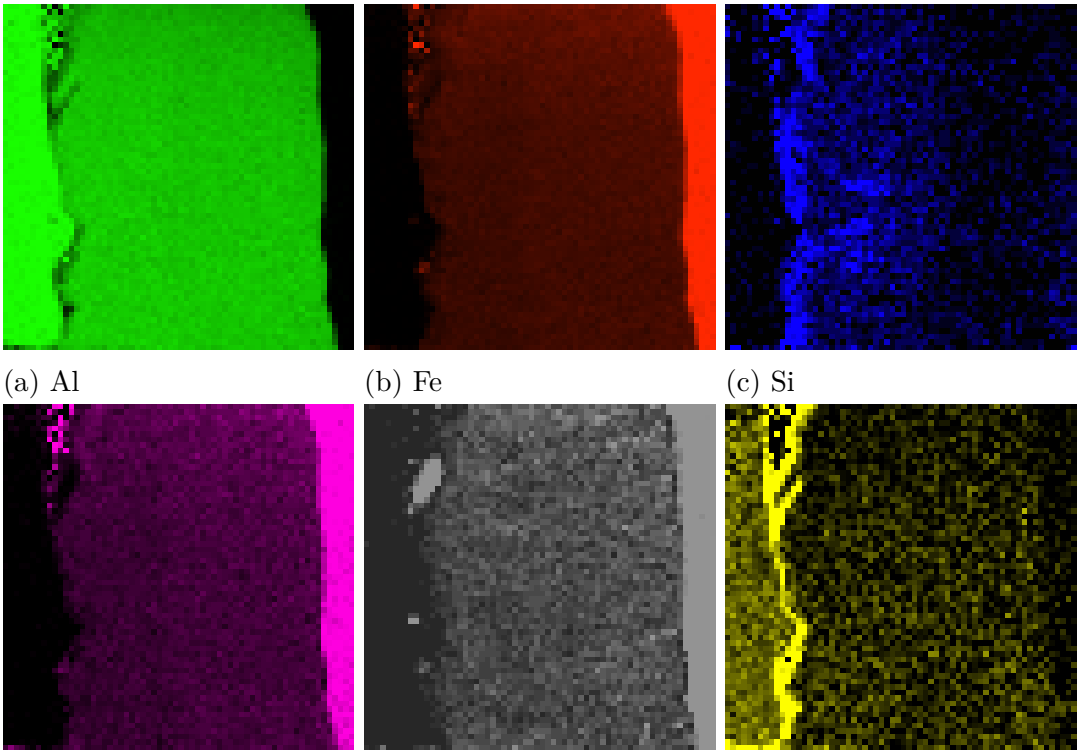

(a) Al (b) Fe (c) Si

(d) Cr (e) Ni (f) O

Figure 4.32: EDS maps of the Al-steel interface after isothermal annealing.

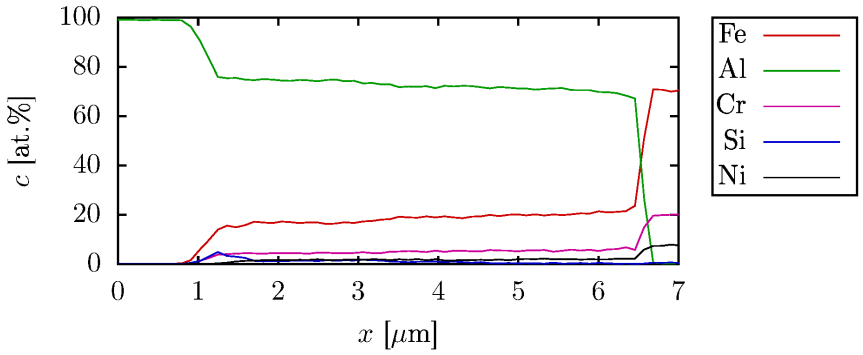

(a) Concentration evaluation without O-content

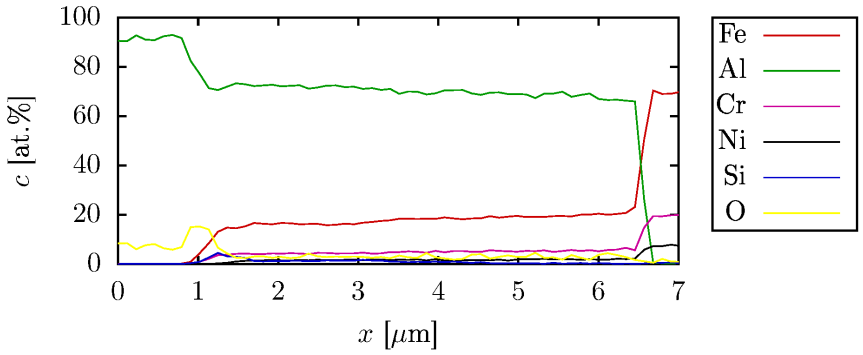

(b) Concentration evaluation with O-content

Figure 4.33: EDS line analysis through Al-steel interface after isothermal annealing.

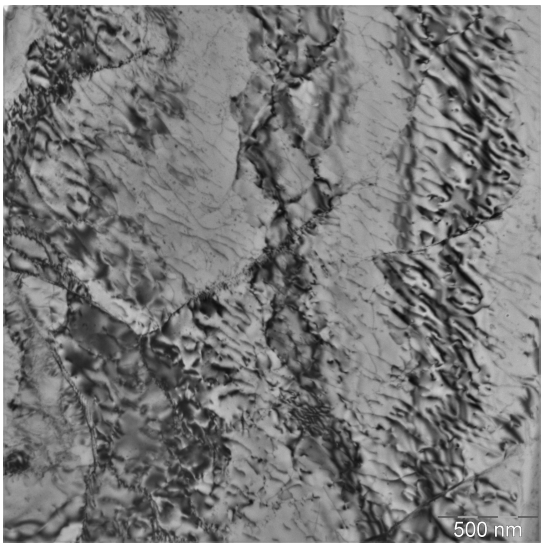

(a) BF image, Al

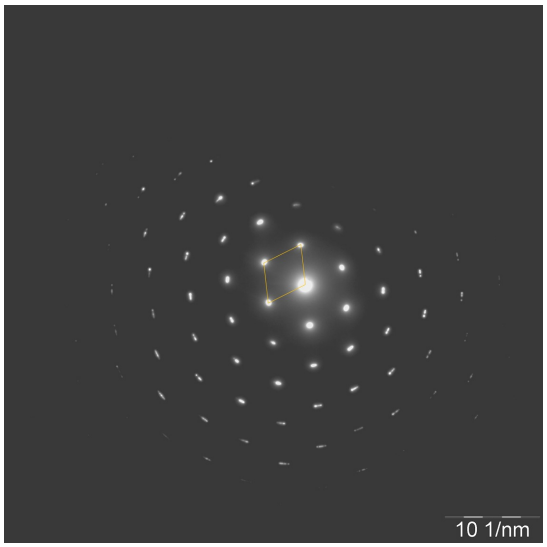

(b) SAED, Al

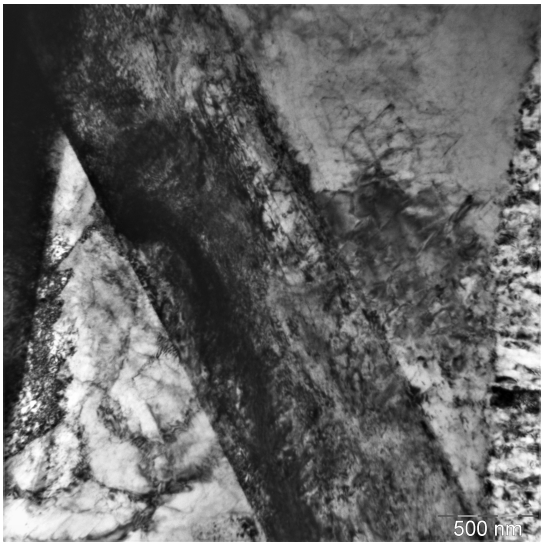

(c) BF image, steel

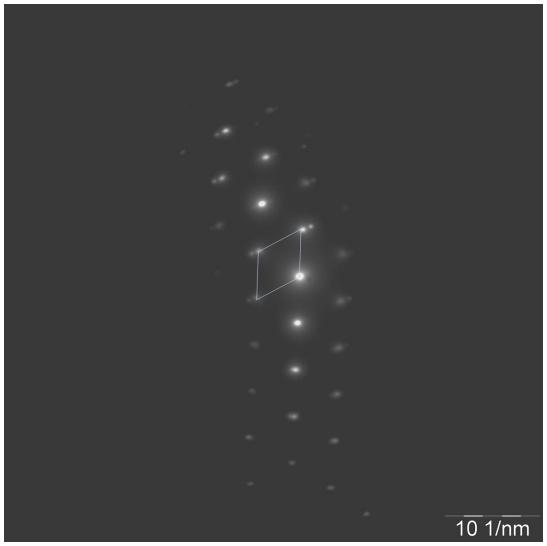

(d) SAED, steel

Figure 4.34: TEM BF images with corresponding SAED patterns

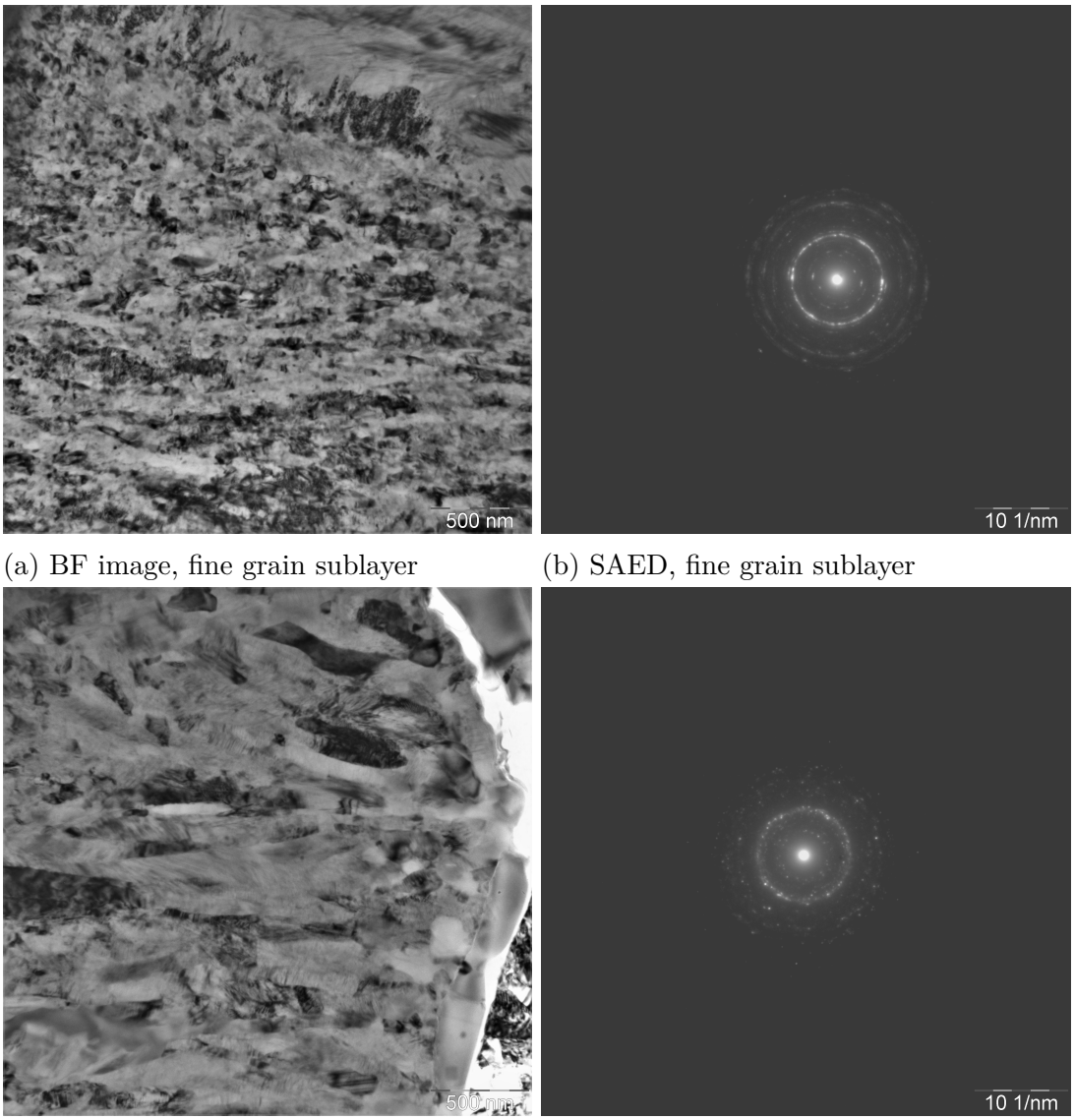

(a) BF image, fine grain sublayer (b) SAED, fine grain sublayer

(c) BF image, columnar grain sublayer (d) SAED, columnar grain sublayer

Figure 4.35: TEM BF images with corresponding SAED patterns

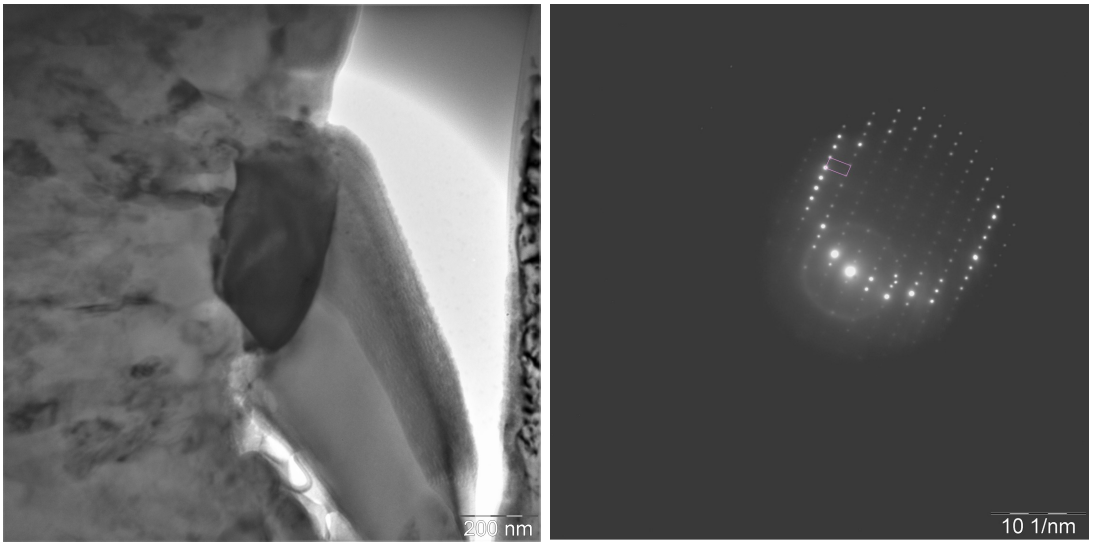

(a) BF image, particle near Al (b) SAED, particle near Al

Figure 4.36: TEM BF images with corresponding SAED patterns

Discussion

5.1 Effect of annealing on electrical resistivity

Absolute value of the electrical resistivity of individual monomaterials and the clad composite were determined by a procedure described by Manesh [52]. A comparison between a theoretical and measured resistivity value of the clad material was done for each temperature and annealing time in order to reveal the influence of the interfacial layer. A connection between the interfacial layer and the difference between measured and theoretical clad material resistivity is legitimate, because the contribution of the interfacial region to the total resistivity value is not assumed in the calculation of the theoretical resistivity value.

Figure 2.2 shows the computational domain. Its size was determined by the dimensions of the given sample for which the resistivity was calculated. The particular sample shape decides about the spatial distribution of the electrical potential. The inhomogeneities of the electrical field were found around the alligator clamps and the sample legs (see Figure 5.1).

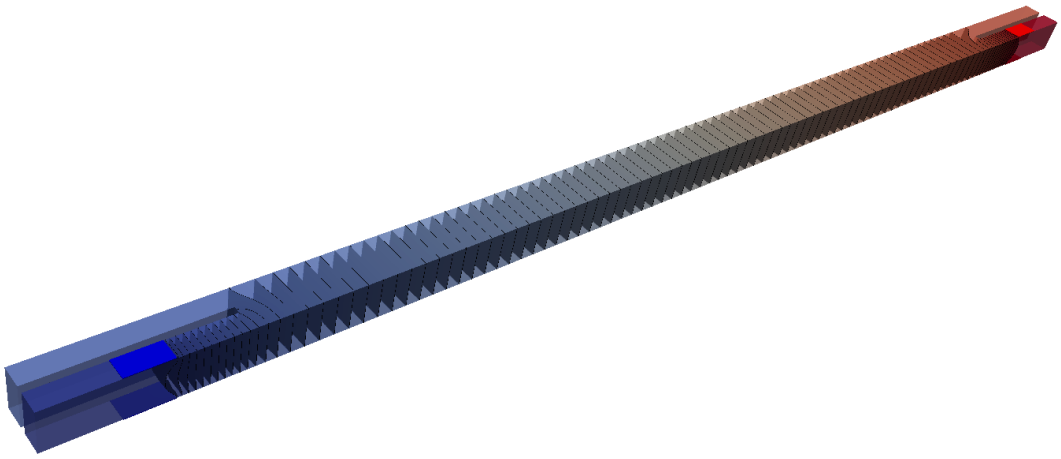

Figure 5.1: FEM simulation of electrical potential distribution. Equipotential planes are displayed through the sample.

Simulated potential course was measured through the H-shape sample between the legs where the voltage was measured after the first calculation with Dirichlet boundary conditions 2.24 (see the red line in Figure 5.2). The potential difference on the ends of the sample was read and compared to that of measured by the voltmeter. Than the Dirichlet boundary conditions were rescaled by the proportion of the measured and calculated voltage so a distribution of electric potential is close to the real one. Calculation of its gradient yields the distribution of the electrical field (the green line in Figure 5.2 shows the longitudinal component of the electric field along the sample).

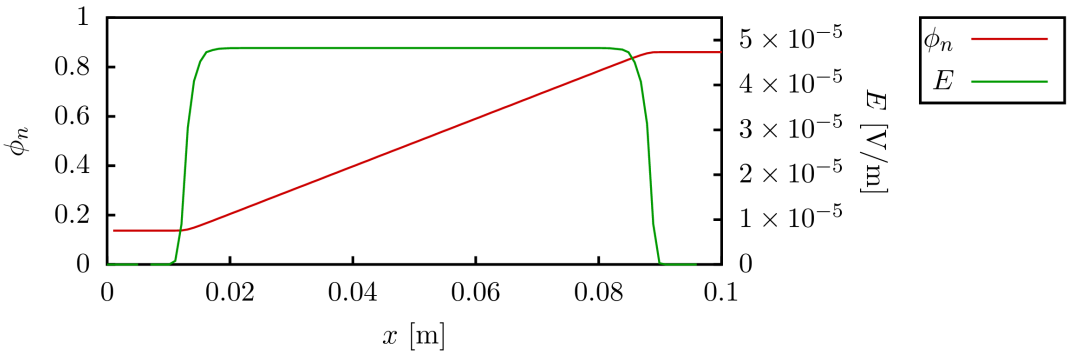

Figure 5.2: FEM simulation of electrical field distribution through the line between the alligators connecting the voltmeter to the sample.

The absolute value of the electrical resistivity was calculated in the central part of the sample from the differential Ohm's law where the electric field has the most homogeneous character (vector E was there completely determined by its longitudinal component) and the current density is simply determined by relation 2.25.

Application of this procedure to all investigated samples in all annealing states allowed to estimate the evolution of the theoretical resistivity of the clad material. The calculation was carried out in the similar manner as it was done by Manesh [52]. The only difference was in the number of the layers, so the relation 2.14 was changed

$$\frac{1}{\rho_{\text{clad}}} = \frac{v_{\text{Al}}}{\rho_{\text{Al}}} + \frac{v_{\text{steel}}}{\rho_{\text{steel}}}, \tag{5.1}$$

where volume fractions of the individual aluminum and steel layer corresponded to the layer thickness ratio $d_{\text{layer}}/d_{\text{clad}}$.

Width and thickness of the sample was measured by a micrometer caliper in several places. A thickness of the clad layers was measured by the same way since the isochronal annealing lead to the sample decomposition. Even though, there could be some discrepancy in estimations of the layer thickness ratios due to the formation of the intermetallic layer on the Al-steel interface which remained joined to the steel layer after the sample destruction and separation of the two constituent layers. The experimental error is expected to be small as the intermetallic layer thickness is negligible compared to the total clad sheet thickness. Generally, the estimation of the sample dimensions introduces the largest error to the computations - the cast sheet was not perfectly planar so the final

H-sample shape were slightly distorted. Another distortion appeared after a high-temperature annealing as the steel and aluminum layer have a different coefficient of a thermal expansion. However, a possible shifting of either of measured ρ_m or predicted resistivity value ρ_p would be manifested by a similar manner during the whole annealing experiment. The processes occurring in the clad sample and contributing in some way to the measured resistivity, could be observed by calculating of the difference or the fraction of the measured and predicted value of the clad sample resistivity. Since the fraction is a dimensionless quantity, its values are graphically shown in Figures 5.3.

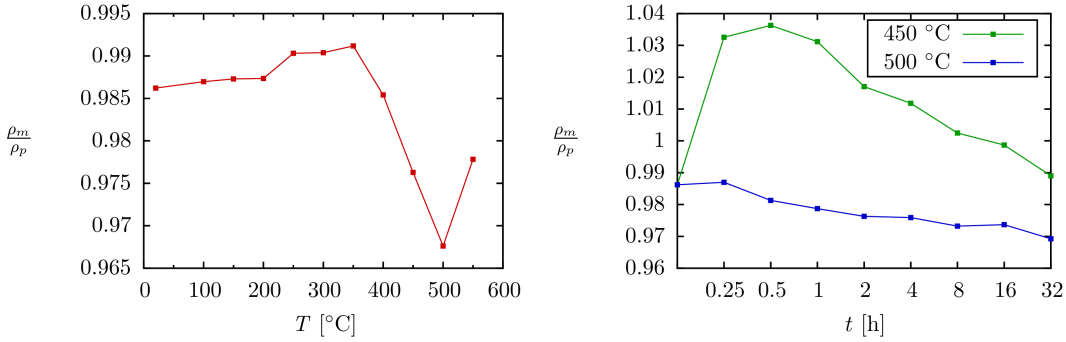

(a) Isochronal annealing (b) Isothermal annealing

Figure 5.3: Fraction of the measured and predicted resistivity of the clad sample.

Graph of the resistivity ratio evolution during isochronal annealing, the ratio increases and approaches one during annealing up to 350 °C. Manesh found a correlation between increase of the bond strength and decrease of the difference between measured and predicted value of the clad sample resistivity. A simmilar trend could be seen in our case. Annealing at mild temperatures could enhance the diffusional process which is on the other side not intensive enough to create the brittle intermetallic phase on the interface so it could result in a development of a diffusional seam and an increase of the bond strength.

Annealing above 350 °C led to a decrease of the resistivity ratio and its retreating from 1. According to Manesh, it could be connected with a degradation of the diffusional seam. Possible increase of the vacancy concentration as a result of different intrinsic diffusion coefficients of Al and Fe atoms (Kirkendall effect) or formation of the brittle intermetallic layer at high temperatures could stand behind the degradation of the joint.

Annealing up to 550 °C causes an increase of the resistivity ratio. Nevertheless, microscopic observation revealed a presence of a thick layer of the intermetallic phase accompanied by the crack formation between the phase and aluminum which could indicate a pronounced deterioration of the bond strength rather than an enhancement of the joint. A potential explanation could be based on the fact, that a massive formation of an ordered structure on the interface could cause a decrease of the overall resistivity because the ordered structures generally evinces higher electrical conductivity in comparison with the ones containing defects.

The interpretation of the results obtained during isochronal annealing experiments could be carried out in the similar way. Annealing for a long time at both temperatures of 450 °C and 500 °C led to a decrease on the resistivity ratio,

which could be related to a progressive deterioration of the bond strength. The excessive increase of the resistivity ratio even far above 1 in the case of annealing at 450 °C did not fully correspond to the resistivity ratio evolution during isochronal annealing. Only an initial increasing trend was maintained with subsequent decrease of the ratio at longer annealing times or higher temperatures. The reason of the sharp resistivity ratio growth would be probably "hidden" in the kinetics of the phase transformations.

5.2 Simulation of the diffusional profile

The Boltzmann-Matano method is one of the simple methods which is used for the determination of a composition dependent interdiffusion coefficient from the concentration-depth profile [65].

First of all, a computation of diffusion coefficient and following simulation were tested at a diffusion profile created with a constant diffusion coefficient, which is the analytic solution of the diffusion equation. Although, the precision of the method is limited near $c = 1$ and $c = 0$, because both of the numerator and denominator in the relation 2.11 tend to zero, the simulation with obtained $D(c)$ shows the satisfactory result of simulation. Diffusion coefficient obtained by Boltzmann-Matano method is compared with the assigned one in the Figure 5.4. Simulation of the concentration profile was done using precisely the calculated diffusion coefficient. The analytic error function overlapps with the resulting simulated profile.

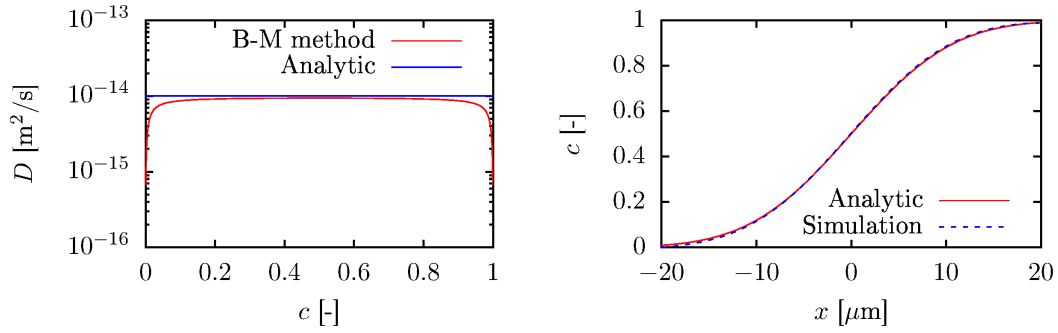

(a) Diffusion coefficient (b) Concentration profile

Figure 5.4: Comparison of given and calculated diffusion coefficient by means of Boltzmann-Matano method with resulting simulation of the concentration profile

Afterwards, the Boltzmann-Matano method was used for the evaluation of $D(c)$ from the measured concentration profiles which were displayed in Figures 4.29. The first obstacle which had to be overcome was the fact, that the system was not a binary system since the aluminum was joined with steel containing a large content of alloying elements. A simplification was done by introducing "atoms of steel" including all elements apart from aluminum. Justification of such step was based on the shape of concentration profiles of Ni and Cr, which were similar to the one of Fe, indicating a similar value of their diffusion coefficients. Si concentration was negligible in comparison with those of other elements.

Diffusion coefficients evaluated from the "steel"-concentration curves were approximated by a piecewise constant function (see Figure 5.5 showing the piecewise fit of $D(c)$ obtained from the 16 h and 32 h lasting annealing). In the case of 4 h and 8 h annealing (Line B and E), a constant value of diffusion coefficient was used. The selected simulations were displayed in Figures 5.6.

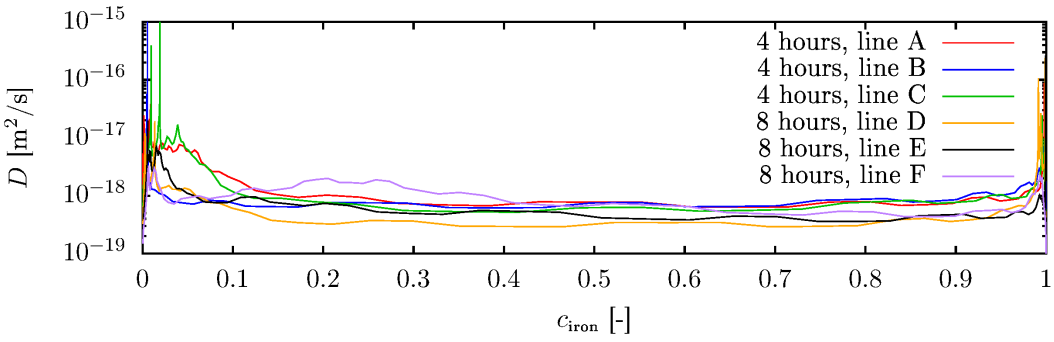

(a) 500 °C / 4 h and 500 °C / 8 h

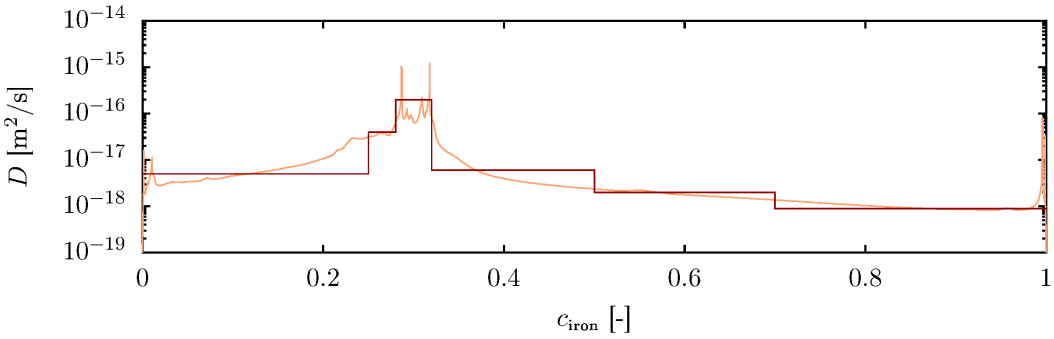

(b) 500 °C / 16 h

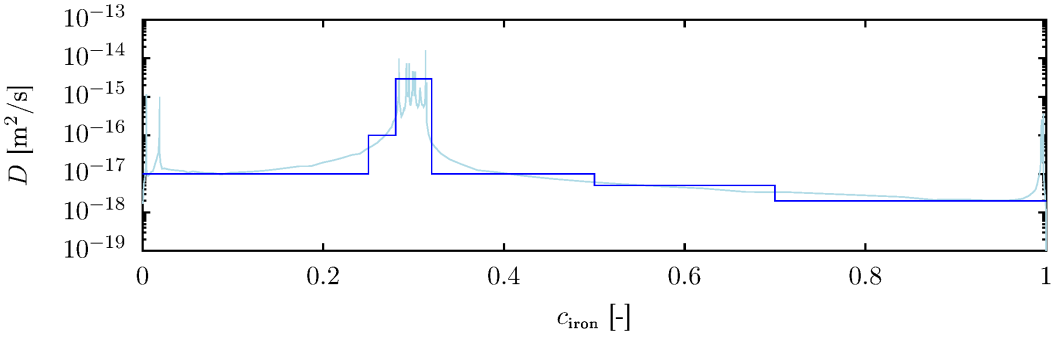

(c) 500 °C / 32 h

Figure 5.5: Diffusion coefficients obtained from diffusion profiles A - H suplemented by a piecewise fit in case of lines G and H

Interpretation of the obtained $D(c)$ is rather confusing. Generally, it represents an effective interdiffusion coefficient, which could in some way quantify the rate of the ongoing diffusion processes. Moreover, when an intermetallic phase forms, probably a different description should be used because the concentration gradient does not have to be the deciding factor.

Another uncertainty arises from the measured concentration profile alone. The diffusion coefficient was calculated from the line profiles obtained by EDS

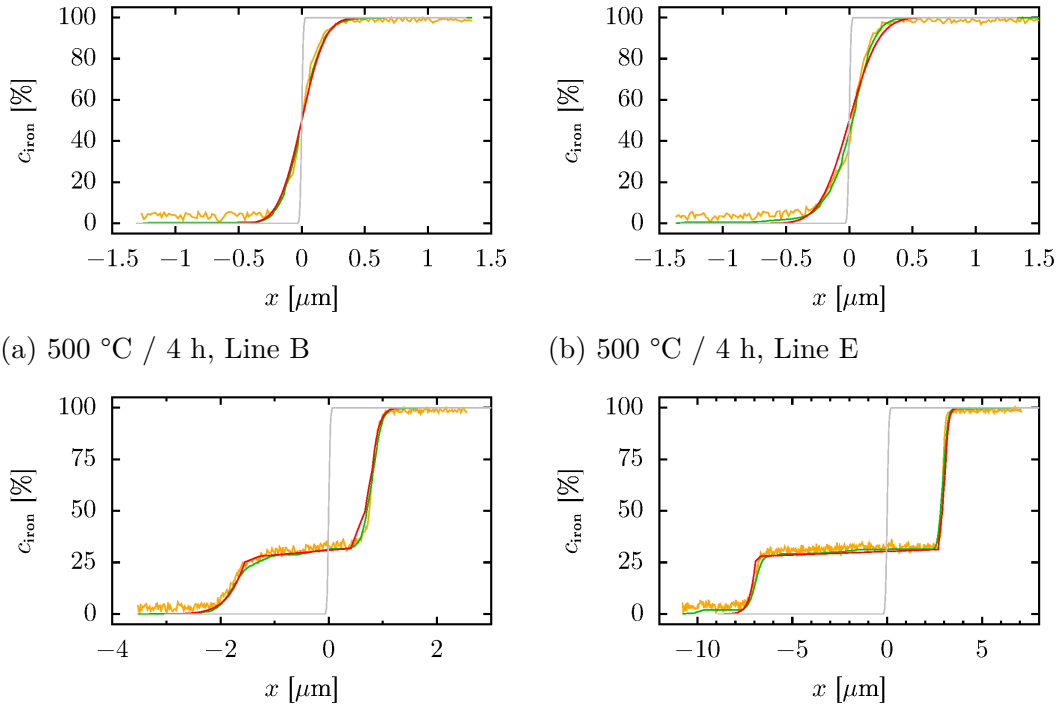

(a) 500 °C / 4 h, Line B

(b) 500 °C / 4 h, Line E

(c) 500 °C / 16 h, Line G

(d) 500 °C / 32 h, Line H

Figure 5.6: Simulations of the selected concentration profiles

analysis in SEM. The problem occurs when the electron beam comes close to the interface. The X-ray signal always comes from a far larger region (so called interaction volume) then it is defined by the electron beam width, because penetrating electrons interacts with the atoms and are spread to all directions. This phenomenon causes that a collected EDS spectrum does not belong to the certain point but includes also information from its nearest vicinity. In the case of measuring the concentration profile through the interface between different phases, it comes about to an averaging of the concentration from the region of the interaction volume. Therefore, measuring of an ideal step-function-concentration profile would show rather error-function shape curve so it could look like a typical diffusion concentration profile. Moreover, since the interaction volume depends also on the atomic number, the shape of the curve could be slightly deformed according to the difference between the volume fractions belonging to the adjacent phases.

In addition, the Boltzmann-Matano's relation is based on the assumption, that concentration profile in $t = 0$ fit to the step-function. However, the samples which were isothermally annealed, did not have to fulfill this condition, because very quick diffusional process probably happened during the twin-roll casting. On the other side, the clad sheet was subjected to a quick cooling due to a rather high casting rate typical for TRC. Furthermore, neither SEM nor TEM observation of the as-cast interfacial region did not revealed a formation of the intermetallic layer, which is closely connected with the diffusion between Al and Fe.

Determination of the diffusion coefficient from the concentration profiles after annealing for 4 h and 8 h shows similar results within a computational error

which support the use of the Boltzmann-Matano method. However, a slight shift of diffusion coefficient determined from the 8h-annealed samples might refer to the mildly developed diffusional seam, because the determination of $D(c)$ from the 4h-anneling was then more developed then it should be. The influence of initial diffuse profile decreased with longer annealing times and pronounced diffusional states.

Longer annealing times revealed the intermetallic phase formation, which manifests itself in increase of the effective interdiffusion coefficient $D(c)$ in concentrations corresponding to the phase composition. Analysis of the concentration profiles after 16 h and 32 h lasting annealing brought similar values of $D(c)$, which support used method again. Moreover, the fact that diffusion did not take place equally along the interface (e.g. 16h-anneale stated also contained regions where no intermetallic phase grew - see Figure 4.28) should be taken into consideration which also could explain the small discrepancies in determination of $D(c)$.

In all simulated profiles shown in Figures 5.6, the initial condition $c(x, t = 0)$ (i. e. the initial position of the interface) is plotted by a grey line. Its correctness remained slightly unclear, because there still persist a question of the applicability of Boltzmann-Matano method, since the condition of the proportionality of gradients of chemical potential and concentration is presented to be fulfilled only in dilute systems and ideal solid solutions.

5.3 Microstructure

Initial microstructure of the aluminum contained a fine dendritic structure in its outer parts with recrystallized equiaxed grains in the strip center (Figure 4.20 a). The observations were in agreement with those of Stolbchenko and Grydin [36, 2]. Steel substrate consisted of equiaxed austenitic grains which remain unchanged during all annealing experiments since the temperatures were not high enough. Some of the grains contained annealing twins (see detail in Figure 4.34 c). Steel microstructure was displayed in Figures 4.3 and 4.21 and will be studied in more detail in the future work. No continuous intermetallic layer was found on the interface of aluminum and steel. Probably a very thin diffusion seam formed, however, a corresponding concentration gradient should be determined by a different method than EDS in SEM due to the concentration averaging caused by overlapping of the interaction volumes.

Isothermal annealing at 500 °C revealed a parabolic growth of the interfacial phase which was observed by many authors dealing with the post-heat treatment of the Fe-Al or steel-Al clad sheets [3, 66, 67]. The layer consisted of several sublayers - the different contrast was obtained in SEM and a miscellaneous grain structure was observed in the layer in TEM depending on a distance from the parent materials. Close to aluminum a very thin layer was found, then a columnar grain structure followed. A fine equiaxed grains of the intermetallic phase were found in sublayer adjacent to steel. The orthorhombic Al_5Fe_2 phase was identified as one of its main constituent confirming the results obtained by different authors [67, 1, 3, 66] (see Figures 4.22 b), 4.35 b). Also a presence of the orthorhombic $Al_{13}Fe_4$ was proved by means of EBSD (Figure 4.35 c).

Longer annealing times at high temperatures resulted not only in a pronounced intermetallic layer growth but moreover, a void formation or cracking

between aluminum layer and the interfacial phase was detected. Two possible reasons leading to such delamination are Kirkendall effect or differences in thermal expansion coefficients of aluminum, intermetallic layer and steel. Varying diffusion coefficients of Al and Fe cause imbalanced mass flux and so result in a formation of Kirkendall's pores on the side of the faster diffusing element. Different thermal expansivity connected with the brittleness of the thick intermetallic would have a similar effect of the clad sheet decomposition. There are both types of studies - some authors tend to the explanation by Kirkendall's effect [3] and some of them prefer the other one using the argument of different thermal expansion [37].

Up to now, all the results were approximately similar with those found in literature. A discrepancy emerged, when the diffusion coefficient of Al in Fe and that of Fe in Al is discussed. An information that the diffusion coefficient of Fe in Al is much higher than Al in Fe can be found in literature (a detailed table of the coefficients e.g. in [68]). Authors often stated, that particles grew towards the Al layer which automatically indicates that iron atoms diffuse into aluminum and it is in agreement with the inequality of the diffusion coefficients. Post-mortem observation of annealed states in SEM also suggested this trend concerning a "bulging" of the phase particles into aluminum (Figure 4.28). Nevertheless, diffusion investigated in-situ in TEM using the secondary electron mode showed quite a surprising results. The temperature during in-situ heating was increased gradually up to 500 °C. No observable changes occurred up to 480 °C. Reaching the temperature of 500 °C resulted in an abrupt growth of the phase towards steel. Any doubts which could originate from the incorrect determination of the initial interface position could be groundless, since a "carbon mark" was done on the aluminum side of the joint (see Figure 4.24). The intermetallic phase grew in the direction from this mark showing the opposite trend than published by several authors in contemporary literature. The delamination between Al and intermetallic layer was observed just as in the case of post-mortem observation in SEM and TEM.

Conclusion

In this work, the interdiffusion and phase transformations in Al-steel clad material were studied. As-cast microstructure of the aluminum layer was inhomogeneous typical for twin-roll cast material containing colonies of Al-Fe-Si-base primary particles. Microstructure of the steel strip contains austenitic microstructure with a content of annealing twins. Almost no intermetallic layer was found on the Al-steel joint. Rarely, tiny particles of Al-Fe-based intermetallic phase occurred in the seam vicinity.

Diffusion and phase transformations were studied during experimental annealing. Three heating schemes were followed: isochronal step-by-step annealing scheme with step 50 °C / 25 min and two isothermal annealing schemes at 450 °C and 500 °C. First evaluation of the diffusional processes was done by means of electrical resistivity measurement. After each annealing step, resistance of a steel, aluminum and composite sample was measured. Calculation of $\Delta\rho/\rho_0$ and RRR during annealing showed very similar evolutions for the aluminum and the clad sample. It showed a very small contribution of the joint to the overall resistance. Shape of the resistivity annealing spectra was governed mainly by the phase transformations ongoing in aluminum layer. Almost unchanged resistivity value of the steel refers to much higher activation energy which is needed to reach any of the possible phase transformations or microstructural changes.

To reveal the influence of the interface, a calculation of the absolute resistivity value was done using FEM. An effective resistivity value of the clad material was compared with a theoretical value calculated from the individual material resistivities of Al and steel. Evaluation of this difference brings an information about the contribution of the seam to the clad sample resistance because it was not included in the calculation of the theoretical value. Their interpretation should be underlying by a mechanical testing of the bond or further analysis or TEM. However, the results seem to correspond with those of showed by Manesh [52]. The difference between measured and predicted resistivity value of the clad sample increased during annealing at mild temperatures during isochronal annealing. According to Manesh [52], it could be a sign of enhancing of the bond. By contrast, increase of the difference could detect the bond deterioration. Samples annealed at 500 °C were characterized by increasing difference between measured and theoretical resistivity value of the clad. The case of annealing at 450 °C remained slightly unclear. In total, trends of the ratio curves obtained during annealing at 450 °C reproduce those of the curves evaluated during isochronal annealing. However, from all the ratio curves the value 1 was exceeded. Possible explanation could be hidden in the different kinetics of the phase transformations. The problematics will be further studied.

Phase transformation in Al were observed during in-situ annealing in TEM. Firstly, dislocations recovery started around 200 °C followed by partial dissolution of primary particles. New particles of a different shapes were found at 400 °C.

Evolution of the intermetallic layer was studied by means of LOM, SEM and TEM. Orthorhombic phases $Al_{13}Fe_4$ and Al_5Fe_2 were identified. An increased Si content was detected in the intermetallic layer close to Al. TEM analysis revealed various microstructure of the intermetallic layer through its thickness. SEM observation also showed several sublayers distinguished in BSE contrast. Concerning isochronal annealing, an evident growth of the interfacial layer started at 500 °C. Bellow this temperature, almost no intermetallic layer was observed. No phase growth was observed during isothermal annealing at 450 °C. A parabolic growth of the intermetallic layer was then observed in the case of isothermal annealing at 500 °C.

The effective interdiffusion coefficient was evaluated by Boltzmann-Matano method from the measured concentration profile. Simulation of the diffusion with obtained interdiffusion coefficient was then carried out using FEM.

A surprising results were obtained from the in-situ annealing in TEM (SEM). Although, the contemporary literature stated a larger diffusion coefficient of Fe in Al than Al in Fe and several authors presented an idea of the formation of the intermetallic layer towards Al, observations in SE show the opposite direction of the phase growth.

Bibliography

[1] O. Grydin, G. Gerstein, F. Nürnberger, M. Schaper, and V. Danchenko. Twin-roll casting of aluminum–steel clad strips. *Journal of Manufacturing Processes*, 15(4):501–507, 2013.

[2] O. Grydin, M. Schaper, and M. Stolbchenko. *Comparison of Twin-Roll Casting and High-Temperature Roll Bonding for Steel-Clad Aluminum Strip Production*, pages 1225–1230. 2015.

[3] H. Springer, A. Kostka, E.J. Payton, D. Raabe, A. Kaysser-Pyzalla, and G. Eggeler. On the formation and growth of intermetallic phases during interdiffusion between low-carbon steel and aluminum alloys. *Acta Materialia*, 59(4):1586–1600, 2011.

[4] R. Baboian and H. Gardner. *ASM Handbook, Corrosion*, volume 13. ASM International, 1987.

[5] L. Chen, Z. Yang, B. Jha, G. Xia, and J.W. Stevenson. Clad metals, roll bonding and their applications for SOFC interconnects. *Journal of Power Sources*, 152:40–45, 2005.

[6] T. Dabney, G. Johnson, H. Yeom, B. Maier, J. Walters, and K. Sridharan. Experimental evaluation of cold spray FeCrAl alloys coated zirconium-alloy for potential accident tolerant fuel cladding. *Nuclear Materials and Energy*, 21:100715, 2019.

[7] D. Cannon, K.-O. Edel, S. Grassie, and K. Sawley. Rail defects: An overview. *Fatigue & Fracture of Engineering Materials & Structures*, 26:865–886, 2003.

[8] Q. Lai, R. Abrahams, P. Mutton, C. Qiu, A. Paradowska, M. Soodi, T. Roy, and W. Yan. Laser Cladding for Railway Repair: Influence of Depositing Materials and Heat Treatment on Microstructural Characteristics. pages 452–463, 2018.

[9] Q. Lai, R. Abrahams, W. Yan, C. Qiu, P. Mutton, A. Paradowska, M. Soodi, and X. Wu. Influences of depositing materials, processing parameters and heating conditions on material characteristics of laser-cladded hypereutectoid rails. *Journal of Materials Processing Technology*, 263:1–20, 2019.

[10] X. Liu, R. Bai, B. Uy, and H. Ban. Material properties and stress-strain curves for titanium-clad bimetallic steels. *Journal of Constructional Steel Research*, 162:105756, 2019.

[11] B.X. Li, Z.J. Chen, W.J. He, P.J. Wang, J.S. Lin, Y. Wang, L. Peng, J. Li, and Q. Liu. Effect of interlayer material and rolling temperature on microstructures and mechanical properties of titanium/steel clad plates. *Materials Science and Engineering: A*, 749:241–248, 2019.

[12] A.G. Olabi and G. Casalino. 6.05 - Mathematical Modeling of Weld Phenomena, Part 1: Finite-Element Modeling. In S. Hashmi, G.F. Batalha, r J. [Van Tyne] Cheste, and B. Yilbas, editors, *Comprehensive Materials Processing*, pages 101–109. Elsevier, Oxford, 2014.

[13] R. Padmanabhan, M.C. Oliveira, and L.F. Menezes. 5 - lightweight metal alloy tailor welded blanks. In Brad L. Kinsey and Xin Wu, editors, *Tailor Welded Blanks for Advanced Manufacturing*, Woodhead Publishing Series in Welding and Other Joining Technologies, pages 97–117. Woodhead Publishing, 2011.

[14] Manual metal arc welding process. `https://techminy.com/manual-metal-arc-welding-process/manual-metal-arc-welding-process-example/`. Accessed: 2020-04-11.

[15] F. Czerwinski. *Welding and Joining of Magnesium Alloys*. 01 2011.

[16] Quintino. L. 1 - overview of coating technologies. In R. Miranda, editor, *Surface Modification by Solid State Processing*, pages 1–24. Woodhead Publishing, 2014.

[17] S.T. Mileiko. Chapter XI - Hot Pressing. In S.T. Mileiko, editor, *Metal and Ceramic Based Composites*, volume 12 of *Composite Materials Series*, pages 475–515. Elsevier, 1997.

[18] H. Kreye et al. Melting phenomena in solid state welding processes. *Welding Journal*, 56(5):154–158, 1977.

[19] F.T. Mahi and U. Dilthey. Joining of Metals. In *Reference Module in Materials Science and Materials Engineering*. Elsevier, 2016.

[20] W.M. Thomas. Friction stir welding and related friction process characteristics. 05 1998.

[21] R.S. Mishra and Z.Y. Ma. Friction stir welding and processing. *Materials Science and Engineering: R: Reports*, 50(1):1–78, 2005.

[22] C.G. Rhodes, M.W. Mahoney, W.H. Bingel, R.A. Spurling, and C.C. Bampton. Effects of friction stir welding on microstructure of 7075 aluminum. *Scripta Materialia*, 36(1):69 – 75, 1997.

[23] K. Jata and S. Semiatin. Continuous Dynamic Recrystallization During Friction Stir Welding of High Strength Aluminum Alloys. *Scripta Materialia*, 43:9, 2000.

[24] A. Elrefaey, M. Takahashi, and K. Ikeuchi. Preliminary Investigation of Friction Stir Welding Aluminium/Copper Lap Joints. *Welding in the World*, 49:93–101, 2005.

[25] Y. Chen and K. Nakata. Friction stir lap joining aluminum and magnesium alloys. *Scripta Materialia*, 58:433–436, 2008.

[26] K. Kimapong and T. Watanabe. Effect of Welding Process Parameters on Mechanical Property of FSW Lap Joint between Aluminum Alloy and Steel. *Materials Transactions*, 46:2211–2217, 2005.

[27] K. Kimapong and T. Watanabe. Lap Joint of A5083 Aluminum Alloy and SS400 Steel by Friction Stir Welding. *Materials Transactions*, 46:835–841, 2005.

[28] G. Zhang, W. Su, J. Zhang, and Z. Wei. Friction stir brazing: A novel process for fabricating Al/steel layered composite and for dissimilar joining of Al to steel. *Metallurgical and Materials Transactions A: Physical Metallurgy and Materials Science*, 42(9):2850–2861, 2011.

[29] G. Huang, X. Feng, Y. Shen, Q. Zheng, and P. Zhao. Friction stir brazing of 6061 aluminum alloy and H62 brass: Evaluation of microstructure, mechanical and fracture behavior. *Materials & Design*, 99:403–411, 2016.

[30] G. Elatharasan and V.S. Senthil Kumar. An Experimental Analysis and Optimization of Process Parameter on Friction Stir Welding of AA 6061-T6 Aluminum Alloy using RSM. *Procedia Engineering*, 64:1227–1234, 2013.

[31] K. Khaledi, S. Rezaei, S. Wulfinghoff, and S. Reese. Modeling of joining by plastic deformation using a bonding interface finite element. *International Journal of Solids and Structures*, 2018.

[32] E.B. Hudson. Direct casting of sheetlike metal structures, 1936. US Patent No. 2128941.

[33] K.S. Papich. Method of continuously casting composite strip, 1997. US Patent No. 5669436.

[34] Prasada Rao A.K., Kyunghwan Kim, J. Bae, G.T. Bae, Dong Shin, and Nack Kim. Twin-Roll Cast Al-Clad Magnesium Alloy. *Materials Science Forum*, 618-619:467–471, 2009.

[35] J. Bae, Prasada Rao A.K., Kyu Han Kim, and Nack Kim. Cladding of Mg alloy with Al by twin-roll casting. *Scripta Materialia*, pages 836–839, 2011.

[36] M. Stolbchenko, O. Grydin, and M. Schaper. Manufacturing and Characterization of Twin-Roll Cast Aluminum-Steel Clad Strips. *Advanced Engineering Materials*, page 1800454, 2018.

[37] H.R. Akramifard, H. Mirzadeh, and M.H. Parsa. Cladding of aluminum on AISI 304L stainless steel by cold roll bonding: Mechanism, microstructure, and mechanical properties. *Materials Science and Engineering: A*, 613:232–239, 2014.

[38] Stainless steel 304l 1.4307. https://www.thyssenkrupp-materials.co.uk/stainless-steel-304l-14307.html. Accessed: 2020-05-01.

[39] Ryabov et al. *Svarka raznorodnych materialov i splavov - DOHLEDAT KNIHU*. Moskau, 1984.

[40] F. Wagner, I. Zerner, M. Kreimeyer, T. Seefeld, and G. Sepold. Characterization and properties of dissimilar metal combinations of Fe/Al and Ti/Al-sheet materials. *ICALEO*, pages 365–374, 2001.

[41] K.G.F. Janssens, D. Raabe, E. Kozeschnik, M.A. Miodownik, and B. Nestler. *Computational Materials Engineering: An Introduction to Microstructure Evolution*. Elsevier Science, 2010.

[42] A. D. Smigelskas and E. O. Kirkendall. Zinc Diffusion in Alpha Brass. *Trans. AIME*, 171:130–142, 1947.

[43] A. Fick. On liquid diffusion. *The London, Edinburgh, and Dublin Philosophical Magazine and Journal of Science*, 10(63):30–39, 1855.

[44] A.J. Dekker. *Solid State Physics*. MACMILLAN & CO LTD, 1957.

[45] P. Atkins and J. de Paula. *Physical Chemistry*. Oxford University Press, 2006.

[46] H. Mehrer. *Diffusion in Solids*, volume 155. Springer-Verlag Berlin Heidelberg, 2007.

[47] Savitzky-golay filtering. https://www.mathworks.com/help/signal/ref/sgolayfilt.html. Accessed: 2020-05-28.

[48] M. Alnæs, J. Blechta, J. Hake, A. Johansson, B. Kehlet, A. Logg, C. Richardson, J. Ring, M. E. Rognes, and G. N. Wells. The FEniCS Project Version 1.5. *Archive of Numerical Software*, 3, 2015.

[49] Anders Logg, Kent-Andre Mardal, and Garth Wells, editors. *Automated Solution of Differential Equations by the Finite Element Method*, volume 84 of *Lecture Notes in Computational Science and Engineering*. Springer-Verlag Berlin Heidelberg, 2012.

[50] J. Crank and P. Nicolson. A practical method for numerical evaluation of solutions of partial differential equations of the heat-conduction type. *Mathematical Proceedings of the Cambridge Philosophical Society*, 43(1):50–67, 1947.

[51] R. Courant, H. Lewy, and K.O. Friedrichs. *On the partial difference equations of mathematical physics*. New York: Courant Institute of Mathematical Sciences, New York University, 1956.

[52] H. Manesh. Assessment of surface bonding strength in Al clad steel strip using electrical resistivity and peeling tests. *Materials Science and Technology*, 22:634–640, 2006.

[53] Material properties, EN AW-1070. https://www.makeitfrom.com/material-properties/1070A-O-Aluminum. Accessed: 2020-03-24.

[54] Stainless Steel Type 304-304L. https://rolledmetalproducts.com/stainless-steel-type-304-304l/. Accessed: 2020-03-24.

[55] O. Grydin, Y.K. Ogins'kyy, V.M. Danchenko, and Fr.-W Bach. Experimental Twin-Roll Casting Equipment for Production of Thin Strips. *Metallurgical and Mining Industry*, 2:348–354, 2010.

[56] M. Stolbchenko, O. Grydin, A. Samsonenko, V. Khvist, and M. Schaper. Numerical analysis of the twin-roll casting of thin aluminium-steel clad strips. *Forschung im Ingenieurwesen*, 78:121–130, 2014.

[57] Q. Wang, X.-s. Leng, T.-h. Yang, and J.-c. Yan. Effects of Fe—Al intermetallic compounds on interfacial bonding of clad materials. *Transactions of Nonferrous Metals Society of China*, 24:279–284, 2014.

[58] M. Hájek, J. Veselý, and M. Cieslar. Precision of electrical resistivity measurements. *Materials Science and Engineering A-structural Materials Properties Microstructure and Processing*, 462:339–342, 2007.

[59] F.C. Schwerer, J.W. Conroy, and Sigurds Arajs. Matthiessen's rule and the electrical resistivity of iron-silicon solid solutions. *Journal of Physics and Chemistry of Solids*, 30(6):1513 – 1525, 1969.

[60] C.H. Yin, Z.H. Gan, S.H. Wang, D.L. Liu, and L.M. Qiu. The Measurement of RRR and Resistance for Aluminum Alloy Based on a Cryocooler. In *Cryocoolers 19*, pages 605–612, San Diego, California, 2016.

[61] M. Cieslar, M. Slámová, J. Uhlíř, C. Coupeau, and J. Bonneville. Effect of composition and work hardening on solid solution decomposition in twin-roll cast al-mn sheets. *Kovove Materialy*, 45:91–98, 2007.

[62] F. Bečvář, J. Čížek, L. Lešták, I. Novotný, I. Procházka, and F. Šebesta. A high-resolution BaF2 positron-lifetime spectrometer and experience with its long-term exploitation. *Nuclear Instruments and Methods in Physics Research Section A: Accelerators, Spectrometers, Detectors and Associated Equipment*, 443(2):557–577, 2000.

[63] J. Čížek, M. Vlček, and I. Procházka. Digital spectrometer for coincidence measurement of Doppler broadening of positron annihilation radiation. *Nuclear Instruments and Methods in Physics Research Section A: Accelerators, Spectrometers, Detectors and Associated Equipment*, 623(3):982–994, 2010.

[64] J. Čížek. Měření doby života pozitronů a jeho využití při studiu kovových materiálů. *Pokroky matematiky, fyziky a astronomie*, 44(3):201–217, 1999.

[65] H. Mehrer, M. Luckabauer, and W. Sprengel. Self- and Solute Diffusion, Interdiffusion and Thermal Vacancies in the System Iron-Aluminium. *Defect and Diffusion Forum*, 333:1–25, 2013.

[66] Ruidi Li, Tiechui Yuan, Xiaojun Liu, and Kechao Zhou. Enhanced atomic diffusion of Fe–Al diffusion couple during spark plasma sintering. *Scripta Materialia*, 110:105–108, 2016.

[67] Jian An, Yongbing Liu, You Lu, and Daren Sun. Hot roll bonding of Al–Pb-bearing alloy strips and steel sheets using an aluminized interlayer. *Materials Characterization*, 47(3):291–297, 2001.

[68] H. Akramifard, H. Mirzadeh, and M. Habibi Parsa. Microstructural Evolution of Roll Bonded Al-Clad Stainless Steel Sheets at Elevated Temperatures. *International Journal of Iron & Steel Society of Iran*, 13(1):38–44, 2016.